

## **Title: A 3D Extra-Large Pore Zeolite Enabled by 1D-to-3D Topotactic Condensation of a Chain Silicate**

**Authors:** Jian Li<sup>1,2,3\*†‡</sup>, Zihao Rei Gao<sup>2,4†</sup>, Qing-Fang Lin<sup>5,6†</sup>, Chenxu Liu<sup>6</sup>, Fangxin Gao<sup>5</sup>,  
Cong Lin<sup>2,3,7</sup>, Siyao Zhang<sup>5</sup>, Hua Deng<sup>8</sup>, Alvaro Mayoral<sup>9,10</sup>, Wei Fan<sup>11</sup>, Song Luo<sup>11</sup>, Xiaobo  
5 Chen<sup>12</sup>, Hong He<sup>8,13</sup>, Miguel A. Cambor<sup>4\*</sup>, Fei-Jian Chen<sup>5,6\*</sup>, Jihong Yu<sup>6\*</sup>

### **Affiliations:**

<sup>1</sup>Berzelii Center EXSELENT on Porous Materials, Department of Materials and  
Environmental Chemistry, Stockholm University; Stockholm, 10691, Sweden.

<sup>2</sup>Anhui ZEO New Material Technology Co.; 778 Dongliu Road, Hefei, 230071, China.

10 <sup>3</sup>College of Chemistry and Molecular Engineering, Peking University; Beijing, China.

<sup>4</sup>Instituto de Ciencia de Materiales de Madrid, Consejo Superior de Investigaciones  
Científicas (ICMM-CSIC); c/Sor Juana Inés de la Cruz 3, Madrid 28049, Spain.

<sup>5</sup>Department of Chemistry, Bengbu Medical College; Bengbu, 233030, China.

15 <sup>6</sup>State Key Laboratory of Inorganic Synthesis and Preparative Chemistry, College of  
Chemistry; International Center of Future Science, Jilin University; Changchun, China.

<sup>7</sup>Department of Mechanical Engineering, The Hong Kong Polytechnic University; Kowloon,  
Hong Kong, China.

20 <sup>8</sup>Center for Excellence in Regional Atmospheric Environment, Key Laboratory of Urban  
Pollutant Conversion, Institute of Urban Environment, Chinese Academy of Sciences;  
Xiamen, 361021, China

<sup>9</sup>Instituto de Nanociencia y Materiales de Aragón (INMA), CSIC-Universidad de Zaragoza;  
Zaragoza 50009, Spain

<sup>10</sup>Laboratorio de Microscopias Avanzadas (LMA-Universidad de Zaragoza); 50018,  
Zaragoza, Spain

25 <sup>11</sup>Department of Chemical Engineering, University of Massachusetts; Amherst, MA 01003,  
USA.

<sup>12</sup>State Key Laboratory of Heavy Oil Processing, China University of Petroleum; Qingdao  
266580, China.

30 <sup>13</sup>State Key Joint Laboratory of Environment Simulation and Pollution Control, Research  
Center for Eco-Environmental Sciences, Chinese Academy of Sciences; Beijing 100085,  
China.

\*Corresponding author. Email: jxpxlijian@pku.edu.cn (J.L.); macambor@icmm.csic.es  
(M.A.C.); feijian@jlu.edu.cn (F.-J.C.); jihong@jlu.edu.cn (J.Y.).

†These authors contributed equally to this work

‡Current address: State Key Laboratory of Coordination Chemistry, School of Chemistry and Chemical Engineering, Nanjing University, Nanjing, 210023 China

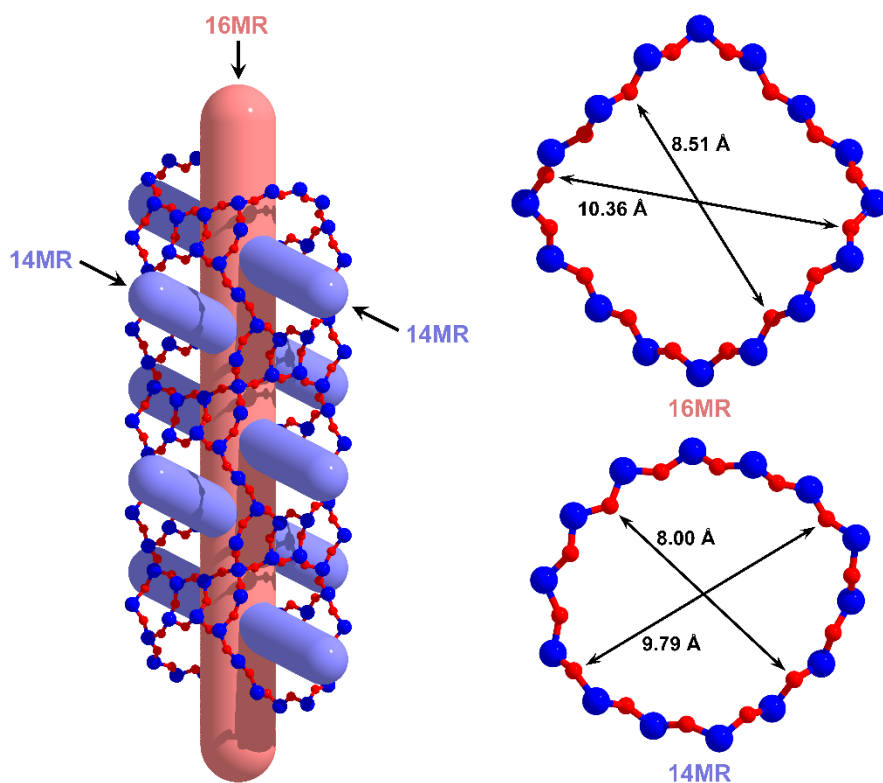
5     **Abstract:** Zeolites are microporous silicates that find an ample variety of applications as  
catalysts, adsorbents, and cation exchangers. Stable silica-based zeolites with increased porosity  
are in demand to allow adsorption and processing of large molecules, but challenge our synthetic  
ability. We report a novel, highly stable pure silica zeolite, ZEO-3, with a multidimensional,  
10     interconnected system of extra-large pores open through windows made by 16 and 14 SiO<sub>4</sub>  
tetrahedra, which is the least dense polymorph of silica known so far. This zeolite was formed by  
an unprecedented one-dimensional to three-dimensional (1D-to-3D) topotactic condensation of a  
chain silicate. With a specific surface area > 1000 square meter per gram, ZEO-3 showed a high  
performance for volatile organic compounds abatement and recovery compared with other  
zeolites and MOFs.

15     **One-Sentence Summary:** ZEO-3, the most porous stable zeolite known so far, shows potential  
in volatile organic compounds abatement and recovery.

**Main Text:**

The size of molecules that can enter, diffuse and react into zeolites are limited by the size of their pores (1-4), which are typically described as "of molecular dimensions", actually meaning of the size of small molecules ( $<7 \text{ \AA}$ ). For many applications, small pores enhance reaction and sorption selectivity (5), but for other applications, such as processing large molecules from petroleum or sorption and reaction of organic pollutants, stable zeolites with larger pores are in demand (6). Natural and synthetic zeolites possess a fully connected three-dimensional network of corner-sharing  $\text{SiO}_4$  tetrahedra; they are tectosilicates or framework silicates (7), with Si occasionally substituted by other atoms. However, some zeolites are obtained in the form of two-dimensional precursors (phyllosilicates or layered silicates) (7) that only become fully connected tectosilicate zeolites by condensation of their layers through a calcination procedure that is "topotactic" because it does not alter the layer topology (8-10). The condensing layers can be obtained by direct synthesis or by disassembly of certain zeolites as in the so-called ADOR (assembly-disassembly-organization-reassembly) process (11).

However, after several decades of extensive and systematic zeolite synthesis studies (12), there have been no reported examples or predictions of a three-dimensional (3D) zeolite obtained by condensation from a one-dimensional (1D) precursor, either directly synthesized or obtained by disassembly of another zeolite. We report such a 1D-to-3D topotactic condensation from ZEO-2, a directly synthesized complex "zeolitic" chain silicate, into ZEO-3, a fully connected 3D extra-large pore zeolite (ZEO-*n* refers to materials discovered and patented by the Anhui ZEO New Material Technology Co., China). This condensation does not alter the topology of the chain silicate, so it is topotactic. The resulting stable zeolite ZEO-3 exhibits very low density, a multidimensional system of interconnected extra-large pores (Fig. 1), and the presence in its structure of double four-membered ring units (D4R), that is, small cubes of silica. For pure silica zeolites, this kind of unit is strained and up to now was believed to need a fluoride anion near its center to be accessible for crystallization (13) because it has never been seen before in a silica zeolite synthesized without the use of  $\text{F}^-$  anions.



**Fig. 1. The extra-large pore system in ZEO-3.** The 3D system of interconnected extra-large pore system (left) and the crystallographic pore size of ZEO-3 (right). The van der Waals radius of O ( $2 \times 1.35 \text{ \AA}$ ) has been subtracted.

5

### Synthesis and structure of the precursor chain silicate

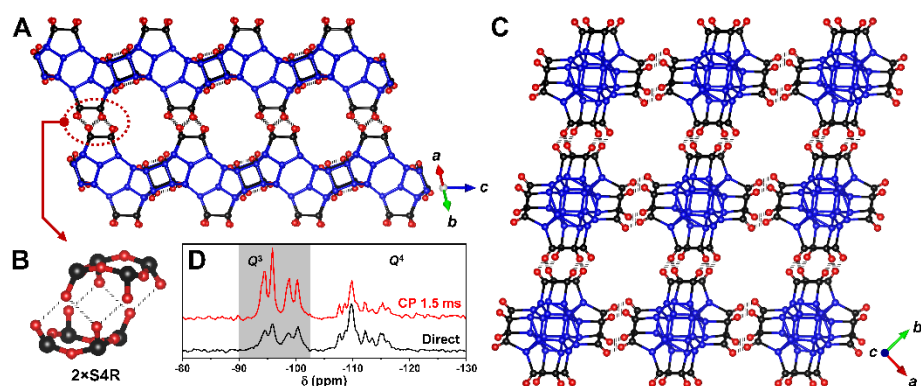
We synthesized the complex chain silica zeolite precursor ZEO-2 using tricyclohexylmethylphosphonium ( $\text{C}_{19}\text{H}_{36}\text{P}^+$ , tCyMP) as an organic structure directing agent (OSDA) from a gel of molar composition  $1 \text{ SiO}_2 : 0.5 \text{ tCyMPOH} : 10 \text{ H}_2\text{O}$  heated at  $175 \text{ }^\circ\text{C}$  (see Supplementary Material). The structure of ZEO-2 was successfully solved ab initio by using eight continuous rotation electron diffraction (cRED) (14) datasets. The pure silicate ZEO-2 crystals display a needle-like morphology (Fig. S1a) and has a *C*-centered monoclinic cell with  $a = 23.5465(7) \text{ \AA}$ ,  $b = 24.7446(7) \text{ \AA}$ ,  $c = 14.4024(4) \text{ \AA}$ ,  $\beta = 115.1974(9)^\circ$  (Tables S1 and S2, Fig. S2). ZEO-2 is a complex 1D chain silicate decorated with silanol and silanolate groups (Fig. 2A) that hold the structure together through numerous hydrogen bonds between adjacent chains (Fig. 2, B and C), with the tCyMP cations located in the interchain space (Fig. S5). The cations were occluded intact, as demonstrated by  $^{13}\text{C}$  and  $^{31}\text{P}$  nuclear magnetic resonance (NMR) (Fig. S6) and amount to 8.85 OSDA per unit cell according to C analysis (25.0 wt%). Hydrogen bonds were observed in the  $^1\text{H}$  magic-angle spinning (MAS) NMR spectrum as a broad resonance around 15.1 parts per million (ppm) (Fig. S7), indicating a moderate-to-strong hydrogen bond (15) corresponding to  $\text{O} \cdots \text{O}$  distances (16) of  $\sim 2.51 \text{ \AA}$ , in good agreement with the crystallographic distances of 2.47 to 2.52  $\text{ \AA}$ .

20

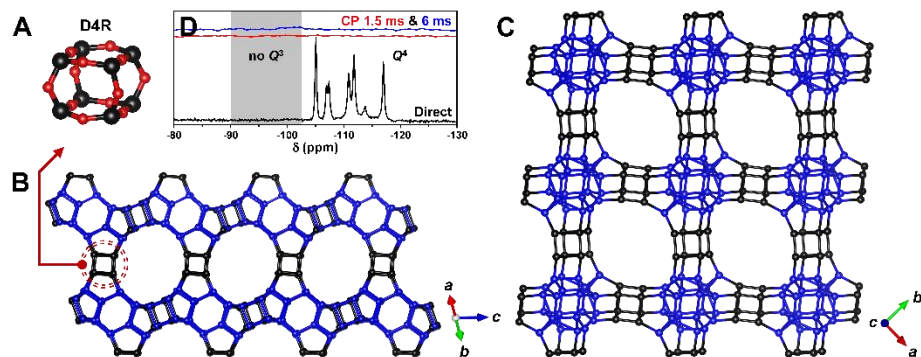
The 1D pure silica chains in ZEO-2 are aligned along the [001] direction (Fig. 2A) and surrounded by four identical chains in the *ab* plane (Fig. 2C). At the edge of the ZEO-2 chain, four silanols or silanolates form a single four-membered ring (S4R) that faced, slightly displaced, an identical S4R from the next chain, with hydrogen bonding along the [110] and [1-10] directions connecting adjacent chains (Fig. 2B). The high resolution of the  $^{29}\text{Si}$  MAS NMR spectrum of ZEO-2 (Fig. 2D), reveals four  $Q^3$  Si sites (-94.2, -95.8, -98.6, and -100.4 ppm) spanning a chemical shift range unprecedented for  $Q^3$  in zeolites, which are more typically centered at around  $\sim -102 \pm 1$  ppm). However, the values are well within the general  $Q^3$  range in silicates (17). The spectrum also shows seven  $Q^4$  Si sites (from -106.8 to -116.8 ppm) and is thus in good agreement with the crystallographic results (4  $Q^3$  and 5  $Q^4$  all with the same multiplicity plus 2  $Q^4$  with half multiplicity, see Table S5).  $^{29}\text{Si}\{^1\text{H}\}$  cross polarization (CP) MAS NMR spectroscopy proved the existence of those four  $Q^3$  Si sites in ZEO-2 (Fig. 2D top).

### Condensation of 1D chains to 3D-extralarge pore zeolite

Upon calcination in air to remove the OSDA (600 °C, 3-hour ramp, 6-hour plateau), silanol groups in adjacent chains condensed into Si-O-Si bridges with H<sub>2</sub>O elimination, resulting in the pure silica zeolite ZEO-3 (Fig. 3, A-C), which maintained the needle-like morphology (Fig. S1b). The condensation occurred between 370 and 390 °C (Fig. S8), coincident with the removal of organics (Fig. S15). Phosphorus residues were eliminated by washing with water within an autoclave at 100 °C for 1 day, or by reduction with H<sub>2</sub> (a mixture of H<sub>2</sub>/N<sub>2</sub> with 10/90 volume ratio) from the as-made ZEO-2 sample at 600 °C with a 2-hour ramp and a 6-hour plateau. The structure of ZEO-3 was also solved ab initio by cRED with five datasets (Tables S2 and S3, Fig. S3). The unit cell of ZEO-3 shrank to  $a = 21.5046(8)$  Å,  $b = 21.2757(8)$  Å,  $c = 14.4638(4)$  Å,  $\beta = 108.7196(1)^\circ$  but maintained the same symmetry as ZEO-2, as well as the topology of the chain. Whereas a 17% contraction of the structure occurred along *a*- and *b*- axis, the *c*-axis underwent only a marginal expansion of 0.4%. To obtain more accurate atomic positions, the structures of ZEO-2 and ZEO-3, including the position of the disordered tCyMP in ZEO-2, were subsequently Rietveld refined against synchrotron powder X-ray diffraction data (SPXRD, Figs. S4 and S5, Tables S4 to S10). All the unit cell data given above correspond to the refined structures. The final refined unit-cell compositions of ZEO-2 and ZEO-3 were [Si<sub>80</sub>O<sub>176</sub>H<sub>24</sub>](C<sub>19</sub>H<sub>36</sub>P)<sub>8</sub> and Si<sub>80</sub>O<sub>160</sub>, respectively (see Supporting Material for details).



**Fig. 2. The structure of the chain silicate ZEO-2.** Only O atoms related to the subsequent condensation reaction are shown (small red spheres). Silicon atoms are shown as blue (always  $Q^4$ ) or black ( $Q^3$  in ZEO-2 converting into  $Q^4$  in ZEO-3). (A) A chain of ZEO-2 is hydrogen bonded (B) to four adjacent chains (C). (D) The  $^{29}\text{Si}$  MAS NMR spectrum (bottom) shows resolution of  $Q^3$  and  $Q^4$  silicon sites (4 and 7 sites, respectively). The close proximity of  $Q^3$  sites to H atoms is revealed in the  $^{29}\text{Si}\{^1\text{H}\}$  CP MAS NMR spectrum by their relative intensity enhanced by polarization transfer from close protons at short contact time (top, 1.5 ms).

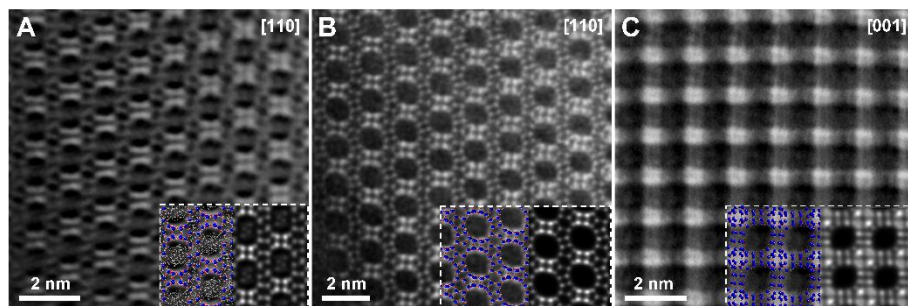


**Fig. 3. The 1D-to-3D topotactic condensation into the extra-large pore framework silicate ZEO-3.** (A) During calcination of ZEO-2, condensation of  $Q^3$  sites through dehydroxylation connects two S4Rs to make a D4R, through which each chain is bonded to four adjacent chains, resulting in the extra-large pore ZEO-3 with 14MR (B) and 16MR (C) channels. (D) The corresponding  $^{29}\text{Si}$  MAS NMR spectrum (bottom) is dominated by  $Q^4$  sites with almost no  $Q^3$  defects and hence little intensity enhancement in the  $^{29}\text{Si}\{^1\text{H}\}$  CP MAS NMR under short (middle, 1.5 ms) or long contact times (top, 6 ms).

During thermal treatment, neighboring S4Rs in ZEO-2 connect to each other to form a D4R (Fig. 3A) by condensation of the terminal Si-OH groups, yielding the fully-connected framework of ZEO-3 (Fig. 3, B and C). The condensed solid is a true, non-interrupted, three-dimensional extra-large pore zeolite. The channel system of ZEO-3 is 3D with  $16 \times 14 \times 14$  membered-ring (MR) channels (Fig. 3, B and C) and full connectivity between channels (Fig. 1). The fulfillment of the condensation process is demonstrated by the  $^{29}\text{Si}$  MAS NMR spectrum of ZEO-3, which reveals total condensation: all Si atoms are  $Q^4$  sites (Fig. 3D, bottom) with a negligible amount of  $Q^3$  that could be assigned to connectivity defects, as proved by the very low intensity enhancement by cross polarization (Fig. 3D middle and top) and FT-IR spectra from self-supported pellets (Fig. S16).

The structural models obtained were fully corroborated by spherical aberration (Cs)-corrected scanning transmission electron microscopy (STEM, Figs. 4 and S10) where a faint signal corresponding to the tCyMP (C and P) was also identified between the chains of ZEO-2 (Fig. 4A) in the place that after condensation will become 14MR pores in ZEO-3. The visualization of ZEO-2 along [001] could not be obtained since it was hampered by the larger thickness (since this is the long needle direction) and the existence in the structure of atoms at different  $z$  levels that are displaced from one another along  $x$  and  $y$ . The 14 and 16 MR pores of ZEO-3 are clearly

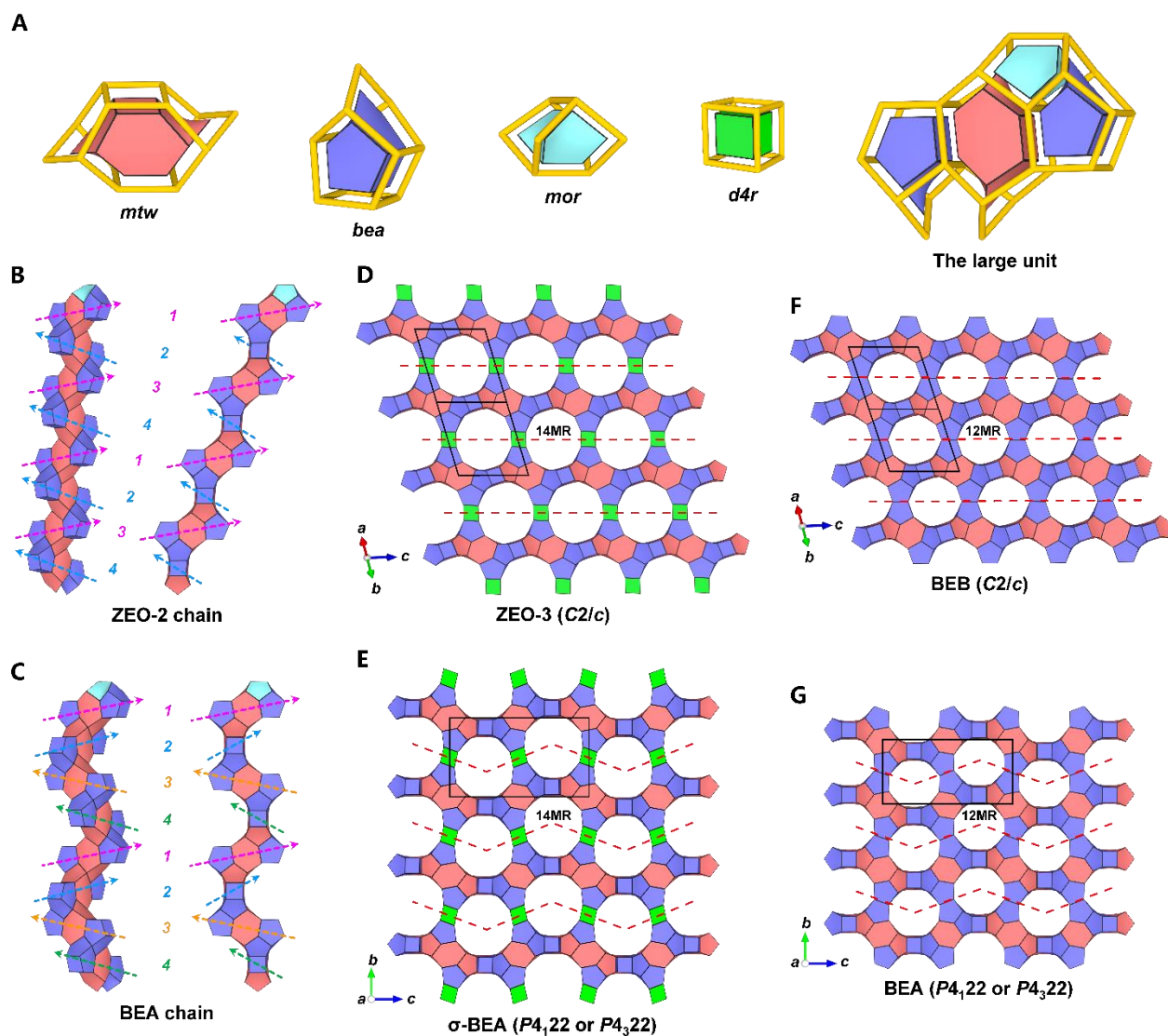
visible (Fig. 4, B and C) together with the smaller 4, 5 and 6R in both materials (Figs. 4 and Fig. S10).



**Fig. 4 Cs-corrected STEM visualization of the 1D silicate chain ZEO-2 and 3D zeolite ZEO-3.** (A) ZEO-2 along [110] projection, and ZEO-3 showing the extra-large (B) 14MR along the [110] and (C) 16MR along the [001] projections. All other rings (4Rs, 5Rs and 6Rs) are clearly visible. To facilitate image interpretation, the schematic models (Si atoms in blue and O atoms in red) have been superimposed and the simulated STEM images are also included in the right bottom inset.

### The $\sigma$ expansion of zeolite Beta polymorphs

The details of the topology are shown in Fig. 5 and Tables S11 and S12. The ZEO-2 chain is topologically identical to the one found in polymorph B of zeolite Beta, although in that zeolite it is not an isolated chain but is embedded in the 3D framework. We use here the acronym BEB to refer to that polymorph, although this is not an accepted zeolite topology code. The chain in BEB and ZEO-3 is built by a large composite building unit (CBU, Fig. 5A) that is alternately rotated by  $+90^\circ$  and  $-90^\circ$  (dotted arrows in Fig. 5B). If the rotation were performed always in the same sense (that is, always by either  $+90^\circ$  or  $-90^\circ$ , dotted arrows in Fig. 5C) a chiral chain would result, which is in fact embedded in the chiral BEA polymorph of zeolite Beta (space group  $P4_122$  or  $P4_322$ ). Thus, condensation of such a chain in a way similar to the condensation of ZEO-2 would result in a new chiral  $16 \times 14 \times 14$ MR hypothetical zeolite. ZEO-3 (Fig. 5D) and this hypothetical chiral zeolite (Fig. 5E) correspond to the  $\sigma$  expansion of polymorphs BEB (Fig. 5F) and BEA (Fig. 5G), respectively, of zeolite Beta (18, 19). A minimization of both structures using the GULP coded suggests the energies of both ZEO-3 and  $\sigma$ -BEA are close to the energy-density relationship normally encountered in zeolites (Fig. S17 and Table S14). Since ZEO-3 has been realized, we believe the hypothetical extra-large pore  $\sigma$ -BEA zeolite might be a reasonable target for future studies.



**Fig. 5. Topology of ZEO-3 and a hypothetical chiral extra-large pore zeolite.** (A) The individual and the large unit CBUs made from them. (B) ZEO-2 chain and (C) BEA chain built by attaching successive large units, viewed along two different directions. The tiling structures of (D) ZEO-3, (E) the  $\sigma$ -expanded BEA, and polymorphs (F) BEB and (G) BEA of zeolite Beta. Dotted arrows indicate topologically identical large units (units 1, 2, 3, 4) rotated by alternating  $+90^\circ$ ,  $-90^\circ$ ,  $+90^\circ$ ,  $-90^\circ$  in B, or non alternating  $+90^\circ$ ,  $+90^\circ$ ,  $+90^\circ$ ,  $+90^\circ$ , or  $-90^\circ$ ,  $-90^\circ$ ,  $-90^\circ$ ,  $-90^\circ$  in C. In D, E, F and G, the dotted lines separate neighbouring ZEO-2 or BEA chains; in D and E, the newly formed D4Rs between neighbouring ZEO-2 or BEA chains are highlighted in green; in F and G, no D4Rs exist as S4R are shared between neighbouring ZEO-2 or BEA chains.

### Properties of ZEO-3

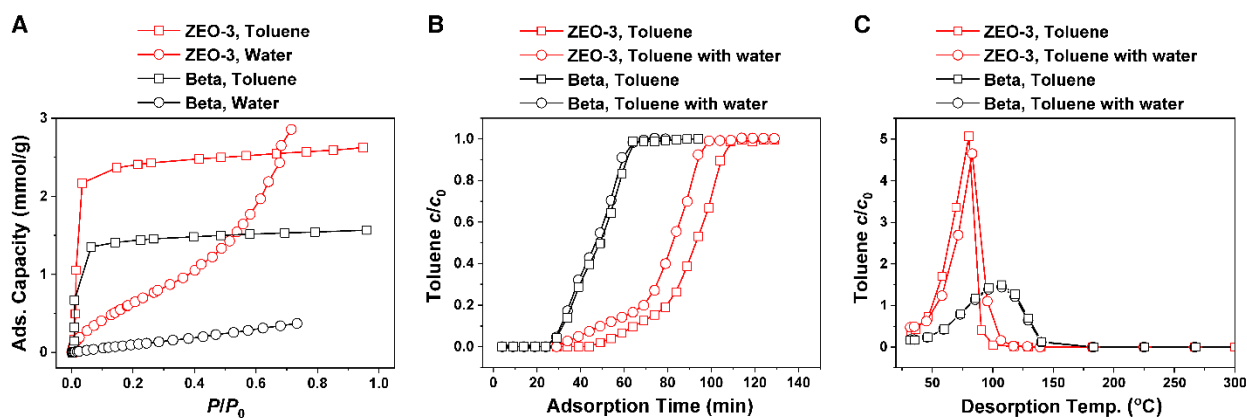
ZEO-3 is a stable, fully-connected silicate zeolite containing 3D interconnected pores opened only through extra-large windows. The crystallographic pore sizes of ZEO-3 are  $10.36 \times 8.51 \text{ \AA}$



and  $9.79 \times 8.00 \text{ \AA}$  for the 16MR and 14MR, respectively (Fig. 1). The 3D extra-large pore nature of ZEO-3 resulted in a very low framework density (FD) value (12.76 tetrahedral atoms, T-atoms, per  $1000 \text{ \AA}^3$ ). Compared with the other known stable, low density (alumino)silicate zeolites, including **FAU**, **EMT**, **\*BEA**, **BEC**, **ISV** and **IWV**, and the recently reported PST-2, PST-32 (20), and ZEO-1 (6), this value is the lowest and puts ZEO-3 as the crystalline silica polymorph with the most open framework (Table S13). The calculated density of ZEO-3 is just  $1.27 \text{ g/cm}^3$ , less than half that of quartz ( $2.65 \text{ g/cm}^3$ ) and near the density of water.

In fact, ZEO-3 breaks the observed tendency between the framework density and the size of the smallest rings in the zeolite structure (21). For an average smallest ring of 4.25, the predicted minimum FD (21) is 13 T-atom per  $1000 \text{ \AA}^3$ , which is greater than the value for ZEO-3. Compared with the real values of non-interrupted zeolites containing 4- and 5-rings, ZEO-3 is well below the lowest calculated FD of **ISV** and **IWV** (15.0; experimental values of 15.4 and 15.7, respectively).

The observed  $\text{N}_2$  and Ar adsorption/desorption isotherms (type Ia) of ZEO-3 revealed high specific surface areas of 989 and  $1032 \text{ m}^2/\text{g}$  (Figs. S11 and S12), respectively. The non-local density functional theory (NLDFT) method applied to the Ar adsorption data calculated mean pore sizes of 10.8 and  $8.8 \text{ \AA}$  (Fig. S13) that match well with the crystallographic results. The extra-large pores of ZEO-3 allowed the diffusion and adsorption of large molecules, like Nile Blue (Fig. S14), suggesting potential for the removal of large organic pollutants from waste liquid streams.



**Fig. 6. Application of 3D extra-large pore zeolite ZEO-3 in volatile organic compounds (VOCs) removal.** VOCs adsorption isotherms (A), breakthrough adsorption (B), and desorption curves (C) on ZEO-3 (red) and Beta (black) zeolite.

Adsorption has been considered as an energy-saving candidate for volatile organic compounds (VOCs) abatement and recovery (22). The development of sorbents with high adsorption capacity, water vapor resistance, and easy regeneration is critical for a successful adsorption technology (23). Zeolites are among the best adsorbents for VOCs given their unique microporosity, high adsorption capacity, and non-flammability (23, 24). The adsorption equilibrium capacities of toluene and water vapor on ZEO-3 were larger than those on Beta,

which has smaller pores (Fig. 6A). ZEO-3 exhibited much longer breakthrough time (better dynamic capacity) than Beta zeolites with little interference from water (Fig. 6B). The main desorption peak of toluene occurred at a lower temperature for ZEO-3 than for Beta (Fig. 6C) making its thermal regeneration easier. Thus, ZEO-3 outperforms Beta, a reference zeolite for this application (25, 26), in terms of adsorption capacity and regeneration potential. Comparison of ZEO-3 with commercial zirconium 1,4-dicarboxybenzene UiO-66, one of the most stable MOFs (27), suggested a similar performance for the fresh materials (Fig. S18). However, after recycling the performance of ZEO-3 was maintained whereas that of UiO-66 was compromised. At the end of five adsorption cycles the PXRD pattern of UiO-66 revealed it had been destroyed while ZEO-3 remained stable (Fig. S19). Additionally, the desorption temperature for UiO-66 was significantly higher than that of ZEO-3 (Fig. S20) indicating a poorer regeneration ability. Phosphorous-free ZEO-3 had a high thermal (1100<sup>0</sup>C 10<sup>0</sup>C/min, 1-hour plateau) and hydrothermal stability (760<sup>0</sup>C, 10% H<sub>2</sub>O, 3 hours) that may ease its application in real conditions (Fig. S9). It is also possible to introduce active sites (such as Ti) into ZEO-3 through a one-pot synthesis method (Figs. S21-S22). Ultraviolet-visible spectra reveal that Ti-ZEO-3 exhibits both tetra- (~210 nm) and hexa-coordinated (~270 nm) Ti species (Fig. S23). Catalytic properties of Ti-ZEO-3 will be investigated in a future work.

### Concluding remarks

Finally, the fact that ZEO-3 presents structural features that sharply depart from previous observations (silica D4R units without F and FD lower than predicted) deserves some consideration. Those previous observations refer to materials directly synthesized by hydrothermal crystallization. The successful synthesis of ZEO-3 demonstrates that materials that may be considered not accessible by direct synthesis can be obtained by post-synthesis transformations, as it has also been observed for zeolites obtained by the ADOR process, which afforded "unfeasible" zeolites (28) or the hybrid guest-host pure silica **STW**, which was also predicted unfeasible by direct synthesis (29). This observation allows to foresee new materials developed by 1D-to-3D topotactic condensation as it has been the case for the ADOR process. It is worth to mention that the final step in the ADOR process is a 2D-to-3D condensation similar to the 1D-to-3D process reported here but which, however, produces a systematic reduction in pore size with regard to the parent material.

### References and Notes

1. J. Zhong, J. Han, Y. Wei, Z. Liu, Catalysts and shape selective catalysis in the methanol-to-olefin (MTO) reaction. *J. Catal.* **396**, 23-31 (2021). doi: 10.1016/j.jcat.2021.01.027.
2. T.-Y. Cui, A. Rajendran, H.-X. Fan, J. Feng, W.-Y. Li, Review on Hydrodesulfurization over zeolite-Based catalysts. *Ind. Eng. Chem. Res.* **60**, 3295-3323 (2021). doi: 10.1021/acs.iecr.0c06234.

3. Y. Wu, B. M. Weckhuysen, Separation and purification of hydrocarbons with porous materials. *Angew. Chem. Int. Ed.* **60**, 18930-18949 (2021). doi: 10.1002/anie.202104318; *Angew. Chem.* **133**, 19078-19097 (2021). doi: 10.1002/ange.202104318.
4. S. Montalvo, C. Huiliñir, R. Borja, E. Sánchez, C. Herrmann, Application of zeolites for biological treatment processes of solid wastes and wastewaters – A review. *Biores. Tech.* **301**, 122808 (2020). doi: 10.1016/j.biortech.2020.122808.
5. M. Dusselier, M. E. Davis, Small-pore zeolites: synthesis and catalysis. *Chem. Rev.* **118**, 5265-5329 (2018). doi: 10.1021/acs.chemrev.7b00738.
6. Q.-F. Lin, Z. R. Gao, C. Lin, S. Zhang, J. Chen, Z. Li, X. Liu, W. Fan, J. Li, X. Chen, M. A. Cambor, F.-J. Chen, A stable aluminosilicate zeolite with intersecting three-dimensional extra-large pores. *Science* **374**, 1605-1608 (2021). doi: 10.1126/science.abk3258.
7. F. Liebau, Nomenclature and structural formulae of silicate anions and silicates. *Structural Chemistry of Silicates*, Springer-Verlag, Berlin, pp. 72 (1985). doi: 10.1007/978-3-642-50076-3\_5.
8. L. Schreyeck, P. Caullet, J.-C. Mougènel, J.-L. Guth, B. Marler, A layered microporous aluminosilicate precursor of FER-type zeolite. *J. Chem. Soc. Chem. Commun.* 2187-2188 (1995). doi: 10.1039/C39950002187.
9. R. Millini, G. Perego, W. O. Parker Jr., G. Bellussi, L. Carluccio, Layered structure of ERB-1 microporous borosilicate precursor and its intercalation properties towards polar molecules. *Microporous Mater.* **4**, 221-230 (1995). doi: 10.1016/0927-6513(95)00013-Y.
10. B. Marler, H. Gies, Hydrous layer silicates as precursors for zeolites obtained through topotactic condensation: a review. *Eur. J. Mineral.* **24**, 405-428 (2012). doi: 10.1127/0935-1221/2012/0024-2187.
11. P. Eliášová, M. Opanasenko, P. S. Wheatley, M. Shamzhy, M. Mazur, P. Nachtigall, W. J. Roth, R. E. Morris, J. Čejka, The ADOR mechanism for the synthesis of new zeolites. *Chem. Soc. Rev.* **44**, 7177-7206 (2015). doi: 10.1039/c5cs00045a.
12. C. S. Cundy, P. A. Cox, The hydrothermal synthesis of zeolites: history and development from the earliest days to the present time. *Chem. Rev.* **103**, 663-702 (2003). doi: 10.1021/cr020060i.
13. C. M. Zicovich-Wilson, M. L. San-Román, M. A. Cambor, F. Pascale, J. S. Durand-Niconoff, Structure, vibrational analysis, and insights into host-guest interactions in as-synthesized pure silica ITQ-12 zeolite by periodic B3LYP calculations. *J. Am. Chem. Soc.* **129**, 11512-11523 (2007). doi: 10.1021/ja0730361.
14. M. Gemmi, E. Mugnaioli, T. E. Gorelik, U. Kolb, L. Palatinus, P. Boullay, S. Hovmöller, J. P. Abrahams, 3D electron diffraction: the nanocrystallography revolution. *ACS Cent. Sci.* **5**, 1315-1329 (2019). doi: 10.1021/acscentsci.9b00394.
15. T. Steiner, The hydrogen bond in the solid state. *Angew. Chem. Int. Ed.* **41**, 48-76 (2002). doi: 10.1002/1521-3773(20020104)41:1<48::AID-ANIE48>3.0.CO;2-U.
16. H. Eckert, J. P. Yesinowski, L. A. Silver, E. M. Stolper, Water in silicate glasses: quantitation and structural studies by <sup>1</sup>H solid echo and MAS-NMR methods. *J. Phys. Chem.* **92**, 2055-2064 (1988). doi: 0022-3654/88/2092-2055\$01.50/0.
17. G. Engelhardt, Multinuclear solid-state NMR in silicate and zeolite chemistry. *TrAC Trends Anal. Chem.* **8**, 343-347 (1989). doi: 10.1016/0165-9936(89)87043-8.

18. R. M. Barrer, *Hydrothermal chemistry of zeolites*, Academic Press, London, pp. 11 (1982).
19. J. V. Smith, Topochemistry of zeolites and related materials. 1. Topology and geometry. *Chem. Rev.* **88**, 149-182 (1988). doi: 0009-2665/88/0788-0149\$06.50/0.
20. H. Lee, J. Shin, K. Lee, H. J. Choi, A. Mayoral, N. Y. Kang, S. B. Hong, Synthesis of thermally stable SBT and SBS/SBT intergrowth zeolites. *Science*, **373**, 104-107 (2021). doi: 10.1126/science.abi7208.
21. G. O. Brunner, W. M. Meier, Framework density distribution of zeolite-type tetrahedrals nets. *Nature* **337**, 146-147 (1989). doi: 10.1038/337146a0.
22. M. Li, Q. Zhang, B. Zheng, D. Tong, Y. Lei, F. Liu, C. Hong, S. Kang, L. Yan, Y. Zhang, Y. Bo, H. Su, Y. Cheng, K. He, Persistent growth of anthropogenic non-methane volatile organic compound (NMVOC) emissions in China during 1990-2017: drivers, speciation and ozone formation potential. *Atmos. Chem. Phys.* **19**, 8897-8913 (2019). doi: 10.5194/acp-19-8897-2019.
23. C. Yang, G. Miao, Y. Pi, Q. Xia, J. Wu, Z. Li, J. Xiao, Abatement of various types of VOCs by adsorption/catalytic oxidation: A review. *Chem. Eng. J.* **370**, 1128-1153 (2019). doi: 10.1016/j.cej.2019.03.232.
24. S. K. P. Veerapandian, N. De Geyter, J.-M. Giraudon, J.-F. Lamonier, R. Morent, The use of zeolites for VOCs abatement by combining non-thermal plasma, adsorption, and/or catalysis: a review. *Catalysts* **9**, 98, (2019). doi: 10.3390/catal9010098.
25. T. Blasco, M. A. Camblor, A. Corma, P. Esteve, J. M. Guil, A. Martínez, J. A. Perdigón-Melón, S. Valencia, Direct synthesis and characterization of hydrophobic aluminum-free Ti-Beta zeolite. *J. Phys. Chem. B* **102**, 75-88 (1998). doi: 10.1021/jp973288w.
26. Z. Zhu, H. Xu, J. Jiang, H. Wu, P. Wu, Hydrophobic nanosized all-silica Beta zeolite: efficient synthesis and adsorption application. *ACS Appl Mater Interfaces* **9**, 27273-27283 (2017). doi: 10.1021/acsami.7b06173.
27. J. H. Cavka, S. Jakobsen, U. Olsbye, N. Guillou, C. Lamberti, S. Bordiga, K. P. Lillerud, A new zirconium inorganic building brick forming metal organic frameworks with exceptional stability. *J. Am. Chem. Soc.* **130**, 13850-13851 (2008). doi: 10.1021/ja8057953.
28. M. Mazur, P. S. Wheatley, M. Navarro, W. J. Roth, M. Položij, A. Mayoral, P. Eliášová, P. Nachtigall, J. Čejka, R. E. Morris, Synthesis of 'unfeasible' zeolites. *Nature Chem.* **8**, 58-62 (2016). doi: 10.1038/nchem.2374.
29. A. Rojas, M. A. Camblor, A pure silica chiral polymorph with helical pores. *Angew. Chem. Int. Ed.* **51**, 3854-3856 (2012). doi: 10.1002/anie.201108753; *Angew. Chem.* **124**, 3920-3922 (2012). doi: 10.1002/ange.201108753.
30. A. Rojas, E. Martínez-Morales, C. M. Zicovich-Wilson, M. A. Camblor, Zeolite synthesis in fluoride media: structure direction toward ITW by small methylimidazolium cations. *J. Am. Chem. Soc.* **134**, 2255-2263 (2012). doi: 10.1021/ja209832y.
31. Z. R. Gao, S. R. G. Balestra, J. Li, M. A. Camblor, HPM-16, a stable interrupted zeolite with a multidimensional mixed medium-large pore system containing supercages. *Angew. Chem. Int. Ed.* **60**, 20249-20252 (2021). doi: 10.1002/anie.202106734; *Angew. Chem.* **133**, 20411-20414 (2021). doi: 10.1002/ange.202106734.
32. J. D. Gale, A. L. Rohl, The general utility lattice program (GULP), *Mol. Simul.* **29**, 291-341 (2003). doi: 10.1080/0892702031000104887.

33. J. D. Gale, Analytical free energy minimization of silica polymorphs, *J. Phys. Chem. B* **102**, 5423-5431 (1998). doi: 10.1021/jp980396p.
34. K.-P. Schroder, J. Sauer, M. Leslie, C. Richard, A. Catlow, J. M. Thomas, Bridging hydroxyl groups in zeolitic catalysts: a computer simulation of their structure, vibrational properties and acidity in protonated faujasites (H-Y zeolites). *Chem. Phys. Lett.* **188**, 320-325 (1992). doi: 10.1016/0009-2614(92)90030-Q.
35. B. W. H. van Beest, G. J. Kramer, R. A. van Santen, Force fields for silicas and aluminophosphates based on ab initio calculations. *Phys. Rev. Lett.* **64**, 1955-1958 (1990). doi: 10.1103/PhysRevLett.64.1955.
36. S. Smeets, B. Wang, E. Hogenbirk, instamatic-dev/instamatic: 1.7.0. (2021). <https://doi.org/10.5281/zenodo.5175957>.
37. W. Kabsch, Integration, scaling, space-group assignment and post-refinement. *Acta. Cryst. Sect. D* **66**, 133-144 (2010). doi:10.1107/S0907444909047374.
38. W. Wan, J. Sun, J. Su, S. Hovmoller, X. Zou, Three-dimensional rotation electron diffraction: software RED for automated data collection and data processing. *J. Appl. Cryst.* **46**, 1863-1873 (2013). doi:10.1107/S0021889813027714.
39. G. M. Sheldrick, Phase annealing in SHELX-90: direct methods for larger structures. *Acta Cryst. A* **46**, 467-473 (1990). doi: 10.1107/S0108767390000277.
40. O. V. Dolomanov, L. J. Bourhis, R. J. Gildea, J. A. K. Howard, H. Puschmann, OLEX2: a complete structure solution, refinement and analysis program. *J. Appl. Cryst.* **42**, 339-341 (2009). doi.org/10.1107/S0021889808042726
41. A. A. Coelho, TOPAS and TOPAS-Academic: an optimization program integrating computer algebra and crystallographic objects written in C++. *J. Appl. Cryst.* **51**, 210-218 (2018). doi: 10.1107/S1600576718000183.
42. S. Smeets, L. B. McCusker, C. Baerlocher, S. Elomari, D. Xie, S. I. Zones, Locating organic guests in inorganic host materials from X-ray powder diffraction data. *J. Am. Chem. Soc.* **138**, 7099-7106 (2016). doi:10.1021/jacs.6b02953.
43. M. W. Deem, R. Pophale, P. A. Cheeseman, D. J. Earl, Computational discovery of new zeolite-like materials. *J. Phys. Chem. C* **113**, 21353-21360 (2009). doi: 10.1021/jp906984z.
44. T. Blasco, M. A. Camblor, A. Corma, J. Pérez-Pariente, The state of Ti in titanoaluminosilicates isomorphous with zeolite Beta, *J. Am. Chem. Soc.* **115**, 11806-11813 (1993). doi: 10.1021/ja00078a020.
45. Cambridge Crystallographic Data Center (CCDC), structure ICSD-153453. <http://www.ccdc.cam.ac.uk>.
46. M.-J. Díaz-Cabañas, P. A. Barrett, M. A. Camblor, Synthesis and structure of pure SiO<sub>2</sub> chabazite: the SiO<sub>2</sub> polymorph with the lowest framework density. *Chem. Commun.* 1881-1882 (1998). doi: 10.1039/A804800B.
47. R. F. Lobo, M. E. Davis, CIT-1: a new molecular sieve with intersecting pores bounded by 10- and 12-rings. *J. Am. Chem. Soc.* **117**, 3766-3779 (1995). doi: 10.1021/ja00118a013.
48. L. A. Villaescusa, P. A. Barrett, M. A. Camblor, ITQ-7: a new pure silica polymorph with a three-dimensional system of large pore channels. *Angew. Chem. Int. Ed.* **38**, 1997-2000, (1999). doi: 10.1002/(SICI)1521-3773(19990712)38:13/14<1997::AID-ANIE1997>3.0.CO;2-U.

49. M. A. Cambor, A. Corma, P. Lightfoot, L. A. Villaescusa, P. A. Wright, Synthesis and structure of ITQ-3, the first pure silica polymorph with a two-dimensional system of straight eight-ring channels. *Angew. Chem. Int. Ed. Engl.* **36**, 2659-2661 (1997). doi: 10.1002/anie.199726591.
- 5 50. A. Cantín, A. Corma, M. J. Diaz-Cabanas, J. L. Jordá, M. Moliner, Rational design and HT techniques allow the synthesis of new IWR zeolite polymorphs. *J. Am. Chem. Soc.* **128**, 4216-4217 (2006). doi: 10.1021/ja0603599.
51. C. Baerlocher, L. B. McCusker, Database of zeolite structures, <http://www.iza-structure.org/databases/>.
- 10 52. B. W. Boal, J. E. Schmidt, M. A. Deimund, M. W. Deem, L. M. Henling, S. K. Brand, S. I. Zones, M. E. Davis, Facile synthesis and catalysis of pure-silica and heteroatom LTA. *Chem. Mater.* **27**, 7774-7779 (2015). doi: 10.1021/acs.chemmater.5b03579.
53. M. A. Cambor, A. Corma, M.-J. Díaz-Cabañas, C. Baerlocher, Synthesis and structural characterization of MWW type zeolite ITQ-1, the pure silica analog of MCM-22 and SSZ-25. *J. Phys. Chem. B* **102**, 44-51 (1998). doi: 10.1021/jp972319k.
- 15

**Acknowledgments:** We thank Dr. Carlos Márquez (ICP-CSIC) for the FT-IR measurements, Dr. Risheng Bai (JLU) for his kind suggestions in the synthesis and characterization on the titanosilicate ZEO-3, M. J. de la Mata (SIDI-UAM) for her expedited help in collecting MAS NMR spectra, and Dr. Agnieszka Ziolkowska (Umeå University) for her help in TEM sample preparation by ultramicrotomy.

20

**Funding:** Financial support from the National Natural Science Foundation of China (grant numbers: 22288101, 21920102005, 21835002, 22271115, 21601004, 21621001, 21776312, 22078364), the National Key Research and Development Program of China (Grant numbers: 2022YFA1503600, 2021YFA 1501202), the 111 project (B17020), the Natural Science Foundation of the Higher Education Institutions of Anhui Province, China (grant numbers: KJ2020A0585), and the Spanish Ministry of Science Innovation (PID2019-105479RB-I00 project, MCIN/AEI/10.13039/501100011033, and RYC2018-024561-I, Spain) is gratefully acknowledged. The cRED data were collected at the Electron Microscopy Center (EMC), Department of Materials and Environmental Chemistry (MMK) in Stockholm University with the support of the Knut and Alice Wallenberg Foundation (KAW, 2012-0112) through the 3DEM-NATUR project. Use of the Advanced Photon Source at Argonne National Laboratory was supported by the U. S. Department of Energy, Office of Science, Office of Basic Energy Sciences, under Contract No. DE-AC02-06CH11357. Additional funding from the European Union's Horizon 2020 research and innovation program under grant agreement No 823717 - ESTEEM3 and the regional government of Aragon (DGA E13\_20R) is also acknowledged.

25

30

35

**Author contributions:** F.-J.C. conceived the project. J.L., M.A.C., F.-J.C., and J.Y. supervised this work. Z.R.G., Q.-F.L., C.L. (Liu), F.G., S.Z., and F.-J.C. performed the synthesis work. J.L. solved the structure and performed Rietveld refinement and framework energy calculations. Z.R.G. analyzed the topology. J.L., Z.R.G., C.L. (Liu), C.L. (Lin), W.F.,

40

S.L., X.C., and M.A.C. carried out the physicochemical characterization. H.D. worked on the VOCs application. A.M. performed the HRSTEM tests. M.A.C. prepared the initial draft. J.L., W.F., M.A.C., F.-J.C., and J.Y. organized the work and the draft. All the authors discussed the results and revised the manuscript.

5 **Competing interests:** J.L., Q.-F.L., Z.R.G., C.L., and F.-J.C. have filed a patent on zeolites ZEO-2 and ZEO-3. J.L., Z.R.G., and C.L. are affiliated with the company holding the rights on that patent.

**Data and materials availability:** The datasets generated during and/or analyzed during the current study are available from the corresponding authors on reasonable request.

10 Crystallographic parameters for the structure of ZEO-2 and ZEO-3 refined against SPXRD and cRED data are archived at the Cambridge Crystallographic Data Center ([www.ccdc.cam.ac.uk/](http://www.ccdc.cam.ac.uk/)) under reference Nos. CCDC 2125815-2125816 (SPXRD data) and CCDC 2125677-2125678 (cRED data).

## Supplementary Materials

15 Materials and Methods

Supplementary Text

Figs. S1 to S23

Tables S1 to S14

References (30–53)

20



## Supplementary Materials for

### A 3D Extra-Large Pore Zeolite Enabled by 1D-to-3D Topotactic Condensation of a Chain Silicate

Jian Li<sup>1,2,3\*†</sup>, Zihao Rei Gao<sup>2,4†</sup>, Qing-Fang Lin<sup>5,6†</sup>, Chenxu Liu<sup>6</sup>, Fangxin Gao<sup>5</sup>, Cong Lin<sup>2,3,7</sup>, Siyao Zhang<sup>5</sup>, Hua Deng<sup>8</sup>, Alvaro Mayoral<sup>9,10</sup>, Wei Fan<sup>11</sup>, Song Luo<sup>11</sup>, Xiaobo Chen<sup>12</sup>, Hong He<sup>8,13</sup>, Miguel A. Camblor<sup>4\*</sup>, Fei-Jian Chen<sup>5,6\*</sup>, Jihong Yu<sup>6\*</sup>

Correspondence to: jxpxlijian@pku.edu.cn (J.L.); macamblor@icmm.csic.es (M.A.C.); feijian@jlu.edu.cn (F.-J.C.); jihong@jlu.edu.cn (J.Y.).

#### **This PDF file includes:**

Materials and Methods  
Supplementary Text  
Figs. S1 to S23  
Tables S1 to S14



## Materials and Methods

### Zeolite syntheses.

*Pure silica ZEO-2.* ZEO-2 was synthesized using the organic structure-directing agent (OSDA) tCyMP<sup>+</sup>, synthesized following a previously reported protocol (6), from a gel of molar composition 0.5 OSDAOH : 1 SiO<sub>2</sub> : 10 H<sub>2</sub>O at 175 °C for 30 days. Specifically, 2.5094 g (12.05 mmol) of TEOS (tetraethylorthosilicate) was mixed and stirred with 33.9454 g (6.002 mmol, *c* = 0.1768 mmol/g) of OSDAOH overnight for the total hydrolyzation and ethanol evaporation. Once the water content reached the target (2.1618 g or 120 mmol water in this case), the whole content was transferred into a 30-mL Teflon-inserted autoclave. The autoclave was maintained at 175 °C for 30 days without rotation. After crystallization, the solid product was collected, washed with water (30 mL × 2) and acetone (30 mL × 1), dried, and finally identified by PXRD and field-emission scanning electron microscopy (FE-SEM) to get the pure ZEO-2 sample (1.020 g; yield: 21.66 g per 100 g gel).

*Condensation of ZEO-2 to ZEO-3.* ZEO-3 was obtained by calcination of ZEO-2 in air at 600 °C, with a 3-hour ramp and a 6-hour plateau. Phosphorous residues could be eliminated by washing with water within an autoclave at 100 °C for 1 day, or by reduction with H<sub>2</sub> (H<sub>2</sub>/N<sub>2</sub>, v/v = 10/90) from the as-made ZEO-2 sample at 600 °C with a 2-hour ramp and a 6-hour plateau. The thermal stability of the P-free ZEO-3 sample was examined by heating at 800, 900, 1000, and 1100 °C (heating rate of 10 °C/min and 1-hour plateau at the target temperature). ZEO-3 was also hydrothermally stable (760 °C, 10% H<sub>2</sub>O, 3 hours). The corresponding PXRD patterns are all shown in Fig. S9.

*Titanosilicate Ti-ZEO-2.* Ti-ZEO-2 was synthesized using the OSDA tCyMP<sup>+</sup>, TBOT (tetra butylorthotitanate) as the titanium source, and following the recipe for ZEO-2, from a gel of molar composition 0.5 OSDAOH : 1 SiO<sub>2</sub> : 0.02 TiO<sub>2</sub> : 10 H<sub>2</sub>O at 175 °C for 30 days. Specifically, 0.6827 g of TBOT was dissolved in 19.7325 g of ethanol to make solution for spare. 0.4230 g (2 mmol) of TEOS was mixed and stirred with 5.6575 g (1 mmol, *c* = 0.1768 mmol/g) of OSDAOH and 500 μL (0.04mmol) of ethanol solution of the TBOT overnight for the total hydrolyzation and ethanol evaporation. Once the water content reached the target (0.3604g or 20 mmol water in this case), the whole content was transferred into a 5-mL Teflon-inserted autoclave. The autoclave was maintained at 175 °C for 30 days without rotation. After crystallization, the solid product was collected, washed with water (30 mL × 2) and acetone (30 mL × 1), dried, and finally identified by PXRD and FESEM to get the pure Ti-ZEO-2 sample.

*Condensation of Ti-ZEO-2 to Ti-ZEO-3.* Ti-ZEO-3 was obtained by calcination of Ti-ZEO-2 under a H<sub>2</sub> atmosphere (H<sub>2</sub>/N<sub>2</sub>, v/v = 10/30) at 600 °C, with a 2-hour ramp and a 6-hour plateau. To remove the possible rest of organic residues, the sample was calcined again in air at 600°C, with a 6-hour ramp and a 6-hour plateau. Finally, it was identified by PXRD and FESEM as a pure Ti-ZEO-3 sample.

Zr-1,4-dicarboxybenzene UiO-66 (CAS number: 1072413-89-8) was purchased from Chemsoon Co. Ltd and it was pre-treated at 120°C for 12 h, as recommended, before adsorption measurements.

### Characterization

ZEO-2 and ZEO-3 were examined by a field-emission scanning electron microscope (SEM, Hitachi S-4800) with an accelerating voltage of 5 kV coated with Au for crystal habit investigation. FESEM was also performed on a JSM-7800F electron microscope. The N<sub>2</sub> and Ar adsorption/desorption isotherms of P-free ZEO-3 were collected at 77 K and 87 K, respectively,

on an Autosorb-iQ system (Quantachrome) after outgassing at 473 K until the pressure rise in the test cell was less than 25 mTorr/min. Pore size distribution was calculated by using NLDFT (nonlocal density functional theory) adsorption model which describes Ar adsorbed onto zeolite with a cylinder pore structure (AsiQwin 5.21, Quantachrome). The specific surface area was determined by the Brunauer-Emmet-Teller (BET) formalism. Thermogravimetric analyses (TGA) of ZEO-2 were carried out on an SDT Q600 TA instrument with a heating rate of 10 °C/min under air flow (100 mL/min). The magic angle spinning (MAS) nuclear magnetic resonance (NMR) spectra for ZEO-2 and ZEO-3 were collected on a Bruker AV-400-WB equipment and the experimental details have been given elsewhere (30). Fourier transform infrared (FT-IR) spectra on the self-supported pellets were collected on a Thermo Nicolet Nexus 670 spectrometer, with the details described in a previous work (31). Elemental analysis of C, H, and N was performed on a LECO CHNS-932 analyser, while the inductively coupled plasma (ICP) for the determination of the Si and P element content was carried on a PERKIN ELMER OPTIMA 2100 DV. Lab powder X-ray diffraction (PXRD) patterns were collected on a Bruker D8 advance diffractometer (Cu K $\alpha$ ). Characterization of the temperature at which the topotactic condensation occurs was realized *ex situ* as follows: 15 mg of as-made ZEO-2 samples in various crucibles were heated from room temperature to each targeted temperature with a heating ramp of 10 °C/min within a Muffle oven under a hood. When the targeted temperatures were reached, the crucibles were taken out, cooled down to RT, and then the PXRD patterns were collected. The UV-vis diffuse reflectance spectra (UV-vis) was recorded on a PerkinElmer Lambda 950 spectrophotometer using the BaSO<sub>4</sub> plate as a reference. Inductively coupled plasma (ICP) atomic emission spectroscopy was performed on a Thermo IRIS Intrepid II XSP atomic emission spectrometer.

#### Framework energy minimization.

The framework energy of ZEO-3, sigma-BEA and highly porous crystalline silica polymorphs, which are summarized in Table S13, were calculated after energy minimization by the General Utility Lattice Program (GULP, gulp-6.0) (32, 33) using the polarizable Sanders-Leslie-Catlow (SLC) interatomic potential (34), with modified oxygen shell charge and the nonpolarizable van Beest-Kramer-van Santen (BKS) interatomic potential (35). The potential parameters are given in Table S14.

### **Supplementary Text**

#### Ab initio structure solution by cRED.

The *ab initio* structure solution of ZEO-2 and ZEO-3 were conducted on the needle-like crystals using JEOL JEM-2100 transmission electron microscope (TEM, Cs: 1.0 mm, point resolution: 0.23 nm) at 200 kV. Before the data collection, a droplet of suspension was transferred onto a copper grid. During the data collection, the goniometer was rotated continuously while the selected-area ED patterns were captured from the individual crystal simultaneously by a quad hybrid pixel detector (QTPX-262k, 512×512 pixels with the size of 55  $\mu$ m, Amsterdam Sci. Ins.) with video mode, using the software *instamatic* script (36). All the ED patterns were recorded under spot size 3 with an exposure time of 0.5 s. Data processing was conducted using the software packages XDS (37) and REDp (38). In order to improve the data completeness, 8 and 5 datasets were collected for ZEO-2 and ZEO-3, respectively. Structure solution was performed using SHELXT (39) with merged and scaled datasets, from which all the

framework atoms (11 Si atoms and 22 O atoms in the asymmetric unit of ZEO-2 and 11 Si atoms and 20 O atoms in the asymmetric unit of ZEO-3) were located directly. Then, the framework was refined using Olex 2 (40), with atomic scattering factors for electrons.

#### 5 Rietveld refinement.

In order to obtain more accurate structures and locate the position of OSDA, Rietveld refinement of ZEO-2 and ZEO-3 were performed against SPXRD patterns, which were collected under 100 K at the 11-BM beamline of the Advanced Photon Source at Argonne National Laboratory, USA, with a wavelength of 0.458086 Å. The structure from cRED data was used as  
10 the initial model for the Rietveld refinement with the software Topas 6.1 (41). Before refinement, an optimization of the framework geometry was performed by using the distance-least-squares algorithm. In the initial stages of the refinement, soft restraints were placed on the Si-O bond distances (1.61 Å) and the Si-O-Si (145°) and O-Si-O bond angles (109°). These restraints were gradually reduced and eventually completely relaxed. The position of OSDA in ZEO-2 was determined by combining simulated annealing and Rietveld refinement using high-resolution synchrotron diffraction data as described previously (42). Shortly, the procedure can be described as follows: (1) refining the framework against the high-angle data only to extract a reliable scale factor, (2) retrieving the residual electron density inside the channel system corresponding to the position of OSDA from the difference electron density map using the whole  
20 dataset, as shown in Fig. S5, (3) the OSDA was introduced into the channel system as a rigid-body to perform the simulated annealing. During the simulated annealing procedure, all the parameters were fixed except the translation and orientation of the OSDA. After obtaining the initial position of the OSDA, all the parameters were opened to refine one by one, such as peak shape, unit cell, instrument parameters, position of the framework atoms, and the torsion angles in OSDA molecule. After several cycles, the restraints were reduced from the refinement. With these processes, the OSDA was settled at the intersection space of the ZEO-2 chains, which matched well with the residual electron density inside the channel system (Fig. S5). The detailed Rietveld refinement results for ZEO-2 and ZEO-3 are placed in Tab. S4.

#### 30 Scanning transmission electron microscopy (STEM).

High-resolution scanning transmission electron microscopy (STEM) was performed in an X-FEG FEI Titan low base equipped with a monochromator for the electron source and a CEOS spherical aberration corrector (Cs-corrected) for the electron probe assuring a 0.8 Å spatial resolution when operated at 300 kV as it was the present case. Sample preparation was done by  
35 deeply crushing the powder using mortar and pestle. To avoid any possible effect of the ethanol on ZEO-2, the crushed powder was directly deposited on the holey carbon Cu microgrid in dry conditions. ZEO-3 was prepared in a similar way but the crushed powder was dispersed in ethanol and few drops of the suspension were deposited onto holey carbon Cu grids. Due to the particular morphology of ZEO-3, the powder was embedded into a resin and ultramicrotomed to facilitate tilting the crystal along [001] zone axis. For imaging, annular bright field and annular dark field detectors (ABF and ADF) were used simultaneously. ABF data was employed for ZEO-2 to visualize the presence of the OSDA, while ADF was used for ZEO-3.

#### 45 Multi-slice STEM simulations.

To simulate the Cs-corrected STEM data we used the QSTEM program ([www.qstem.org](http://www.qstem.org)). The correspondent supercells were created for the distinct materials and orientations. The parameters used were: Cs = 0 mm, Uacc = 300 kV, an inner collection angle of 25 mrad for the

ADF data and 5 to 25 mrad for the ABF; the half-convergence angle used was 15 mrad.

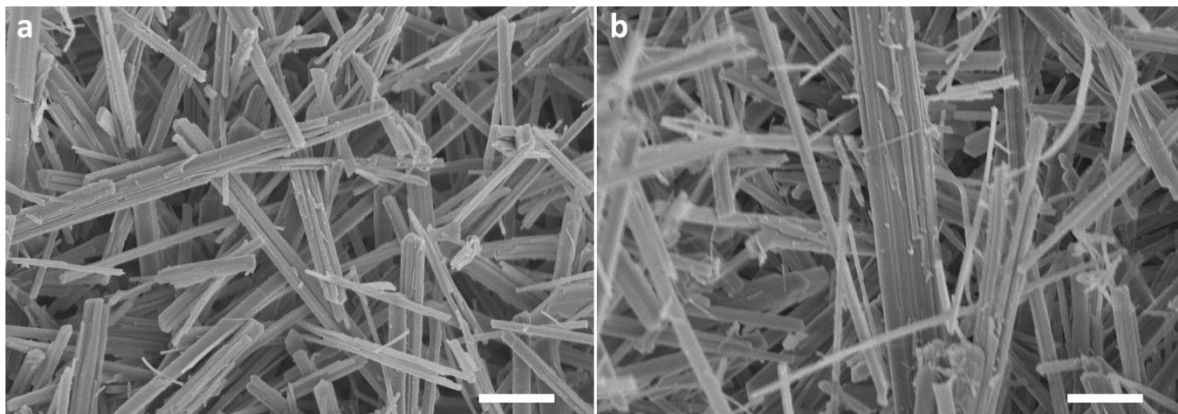
### Dyes Adsorption.

5 Similar to the previous protocols (6), the dye adsorption of Nile Blue (NB, *i.e.* [9-(diethylamino)benzo[a]phenoxazin-5-ylidene]azanium chloride, C<sub>20</sub>H<sub>20</sub>ClN<sub>3</sub>O) was performed on two pure silica zeolites ZEO-3 and Beta. The ultraviolet and visible spectra of several standard NB solution (concentration from 1×10<sup>-4</sup> to 2×10<sup>-6</sup> mol/L) were collected on a UV-2401 PC spectrophotometer. The Lambert-Beer equation for NB at λ = 595 nm within the previous concentration range is: Int (a.u.) = 24214.94305 \* c (mol/L).

### VOC Adsorption.

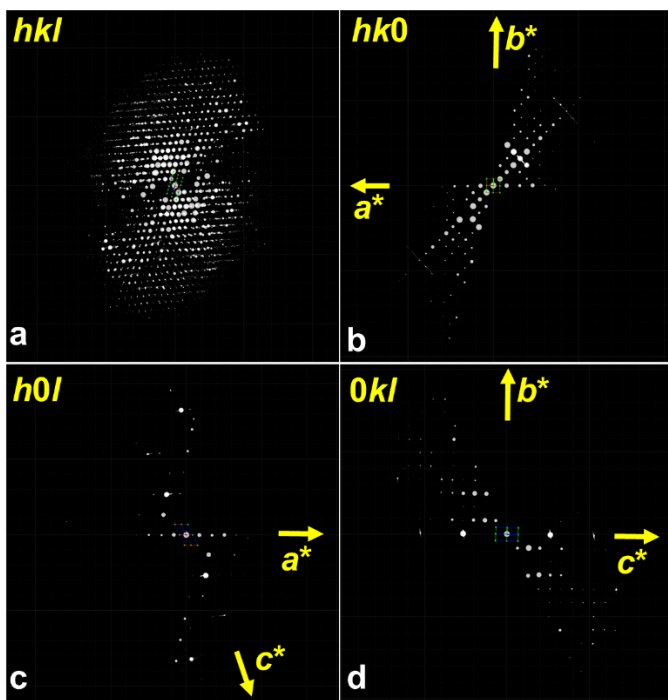
10 In order to determine the adsorption equilibrium, static vapor-phase adsorption was performed using BELSORP-MAX. Each sample was degassed at 300 °C for 3 h. The measurements were carried out at 30 °C to construct the vapor adsorption isotherms. In order to determine the dynamic adsorption behavior, breakthrough measurements were performed in a laboratory-built fixed-bed reactor (6 mm i.d.). A gaseous mixture of C<sub>7</sub>H<sub>8</sub> (about 800 ppm) and water vapor (RH=75±5%, when use) in N<sub>2</sub> balance at a mass flow of 100 mL min<sup>-1</sup> was fed into the reactor at a temperature of 30 °C. A mixture of 0.1 g adsorbent and 0.3 g quartz sand was packed in the bed. Prior to all adsorption measurements, samples were pretreated by purging nitrogen at 300 °C overnight. The concentrations of C<sub>7</sub>H<sub>8</sub> was analyzed online by a gas chromatograph (Kefen, GC-9160, SE-54 capillary column) with a flame ionization detector. Water vapor was tested by humidometer (CENTER 314). To evaluate the regenerability of the adsorbents, temperature-programmed desorption (TPD) measurements were carried out after the breakthrough measurements. Once the samples were saturated by the VOC flow, the feed gas was changed to pure nitrogen to purge for 0.5 h, followed by temperature ramping to 400 °C at a linear rate of 2 °C min<sup>-1</sup>. The product was monitored by the same GC instrument.

20 25 30 35 In order to investigate the stability and reusability of adsorbents, successive adsorption and desorption cycles tests were performed. A mixture of 0.1 g adsorbent and 0.3 g quartz sand was packed in the bed. Prior to all adsorption measurements, ZEO-3 and UiO-66 were pretreated at 300 °C for 3h and 120 °C for 1h, respectively, and then all samples cooled to 30 °C. The feed gas was identical to that in the former single breakthrough test. After the inlet flow reached a constant level, the three-way valve was switched from the bypass to the adsorption column. Then the breakthrough curves could be measured. Once the outlet of toluene was equal to the inlet, the feed gas was changed to pure nitrogen to purge for 0.5 h, followed by temperature ramping to 300 °C at a linear rate of 5 °C min<sup>-1</sup>. The product of desorption by thermal regeneration was monitored by the same GC instrument. Five successive cycles of VOC adsorption and regeneration were performed.



**Fig. S1.**  
**SEM images of (a) ZEO-2 and (b) ZEO-3. The scalebars are 2  $\mu\text{m}$ .**

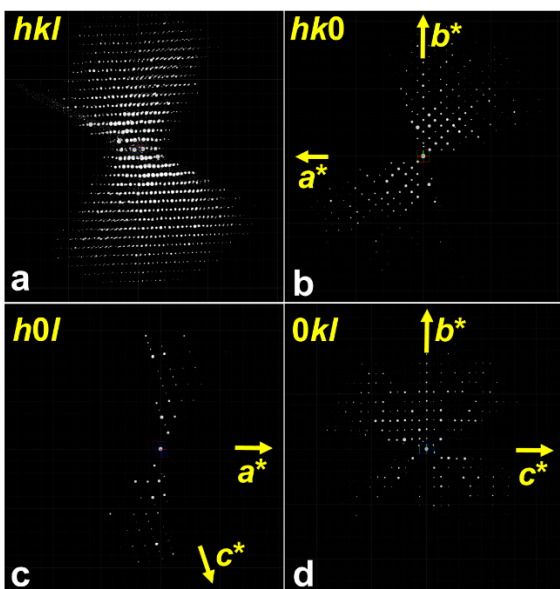
5



**Fig. S2.**

**Typical cRED data (dataset No. 4, Table S1) of ZEO-2.** (a) Projection of the 3D reconstructed reciprocal space. The 2D slices of  $hk0$  (b),  $h0l$  (c), and  $0kl$  (d). The reflection conditions are:  $hk0$ :  $h+k = 2n$ ;  $h0l$ :  $h = 2n, l = 2n$ ;  $0k0$ ,  $k = 2n$ . The determined space group is  $Cc$  (9#) or  $C2/c$  (15#).

5



**Fig. S3.**

**Typical cRED data (dataset No.1, Table S3) of ZEO-3.** (a) Projection of the 3D reconstructed reciprocal space. The 2D slices of  $hk0$  (b),  $h0l$  (c), and  $0kl$  (d). The reflection conditions are:  $hk0$ :  $h+k=2n$ ;  $h0l$ :  $h=2n, l=2n$ ;  $0k0, k=2n$ . The determined space group is  $Cc$  (9#) or  $C2/c$  (15#).

5

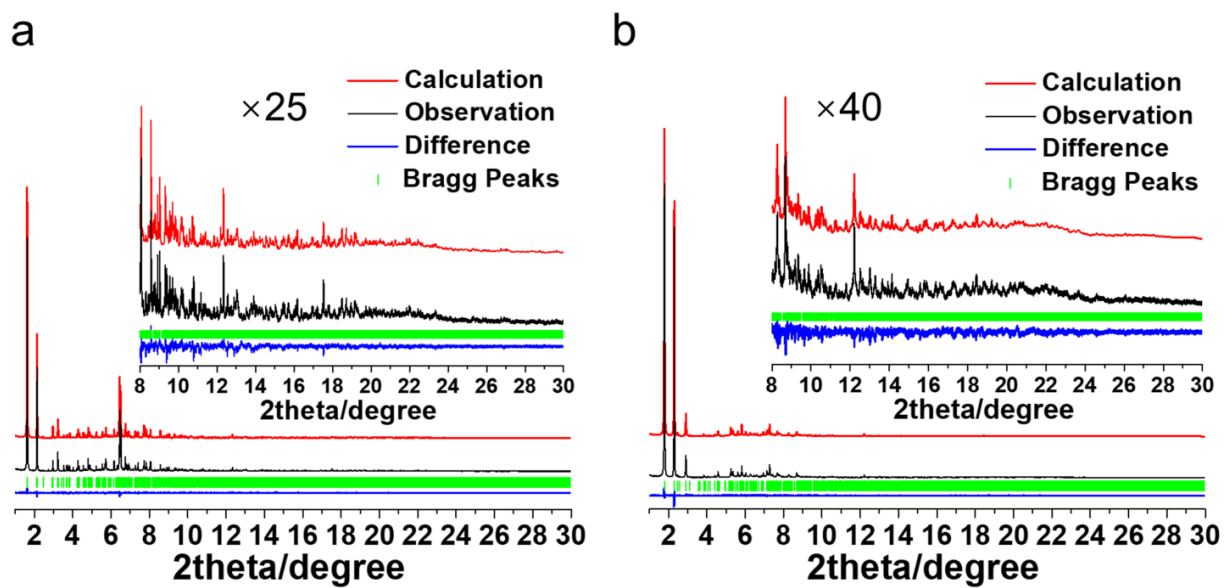
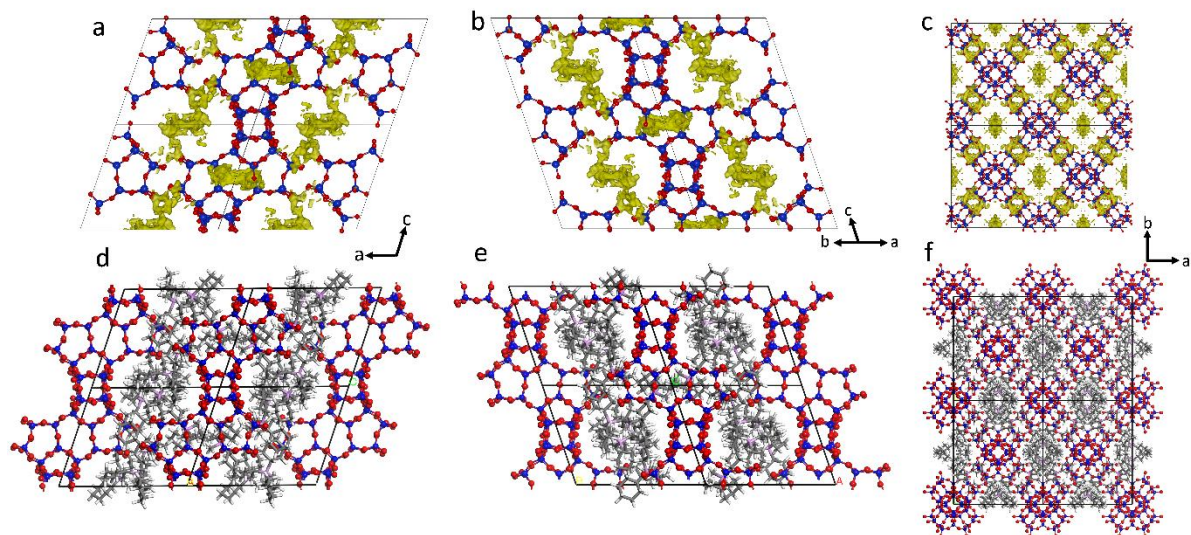


Fig. S4.

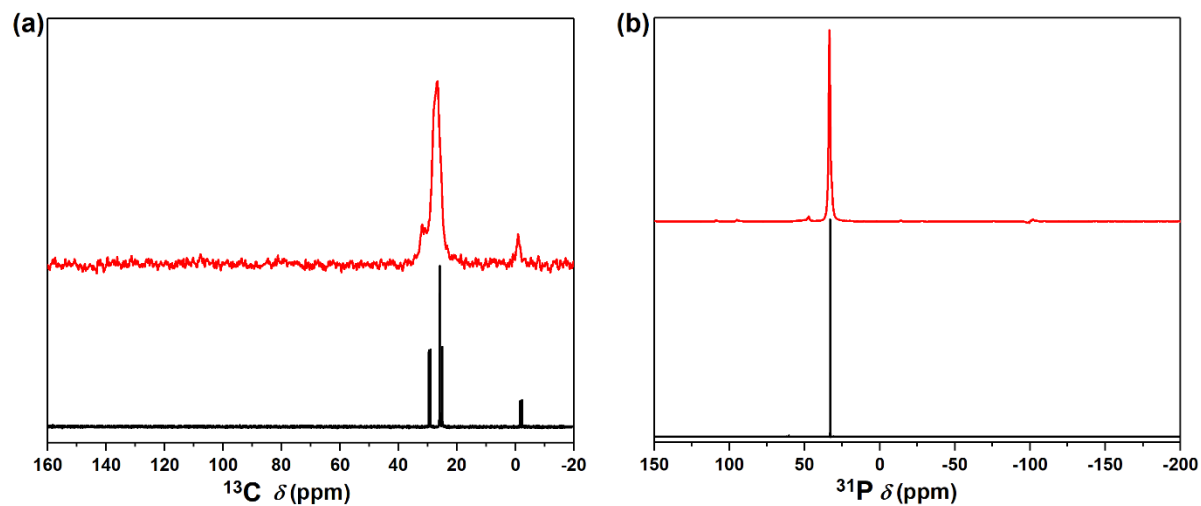
Rietveld refinement plots of (a) ZEO-2 and (b) ZEO-3 ( $\lambda = 0.458086 \text{ \AA}$ ).





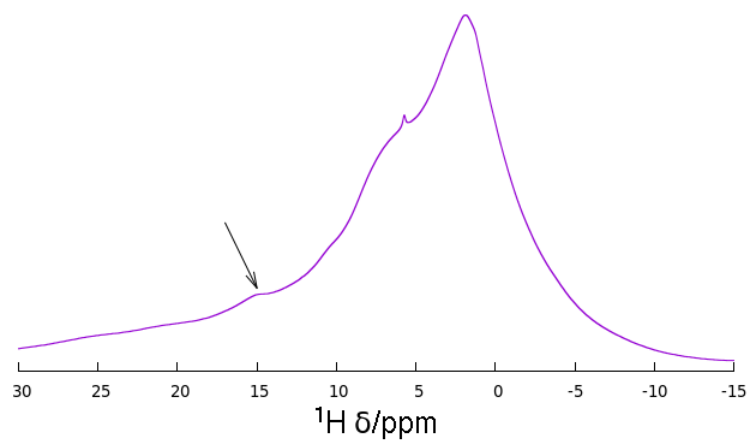
**Fig. S5.**

**Difference electron density maps of ZEO-2.** Views along (a)  $[\bar{1}10]$ , (b)  $[110]$ , and (c)  $[001]$  directions after initial scaling, showing the positive only. Views along (d)  $[\bar{1}10]$ , (e)  $[110]$ , and (f)  $[001]$  directions, showing the location of the tCyMP at the intersection space of the ZEO-2 chains.



**Fig. S6.**

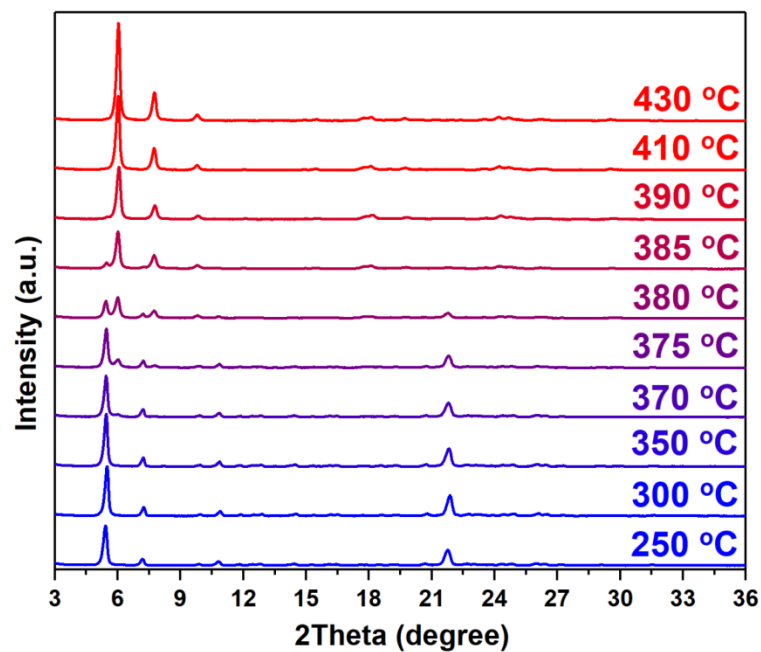
5 (a)  $^{13}\text{C}$  and (b)  $^{31}\text{P}$  NMR spectra of OSDA cation and ZEO-2. Top curves (red) are MAS NMR spectra of the as-made ZEO-2 chain silicate and bottom curves (black) are the liquid NMR spectra of the OSDA chloride dissolved in  $\text{D}_2\text{O}$ , showing the OSDA is intact in ZEO-2.



**Fig. S7.**

**$^1\text{H}$  MAS NMR spectrum of ZEO-2.** The arrow points to a resonance at 15.1 ppm, indicative of the moderate-to-strong hydrogen bonds.

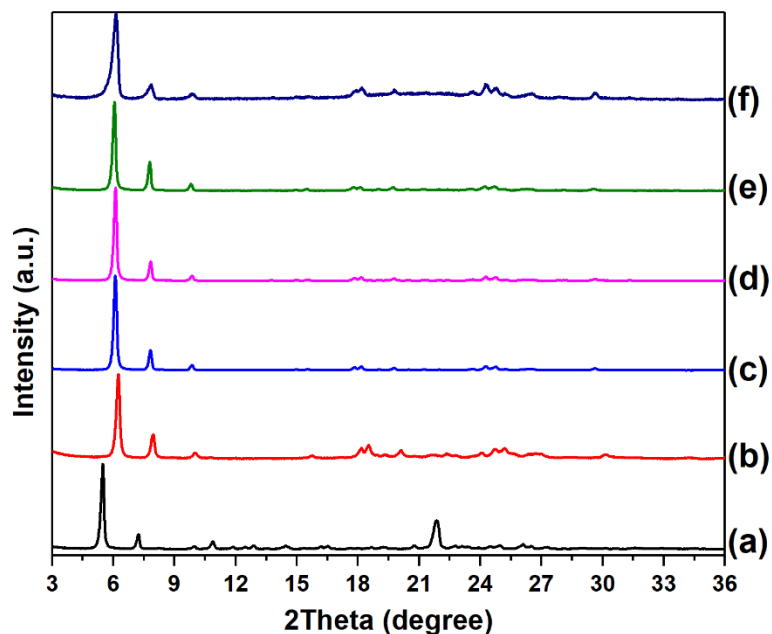
5



**Fig. S8.**

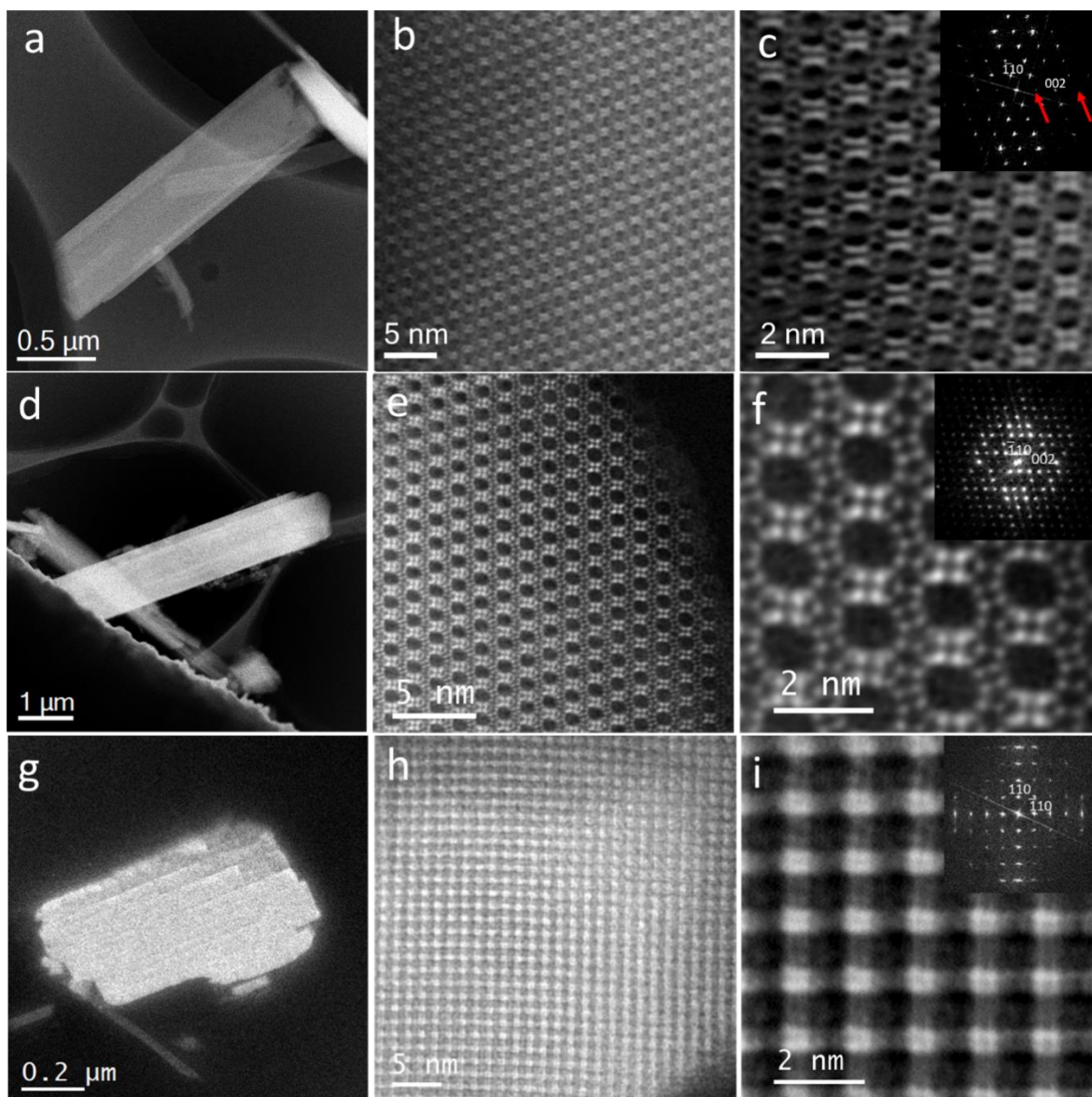
***Ex situ* PXR**D study of the condensation temperature, showing that the process starts around 370 °C and is almost complete at 390 °C, for a 10 °C/min heating ramp (see Materials and Methods for details).

5



**Fig. S9.**

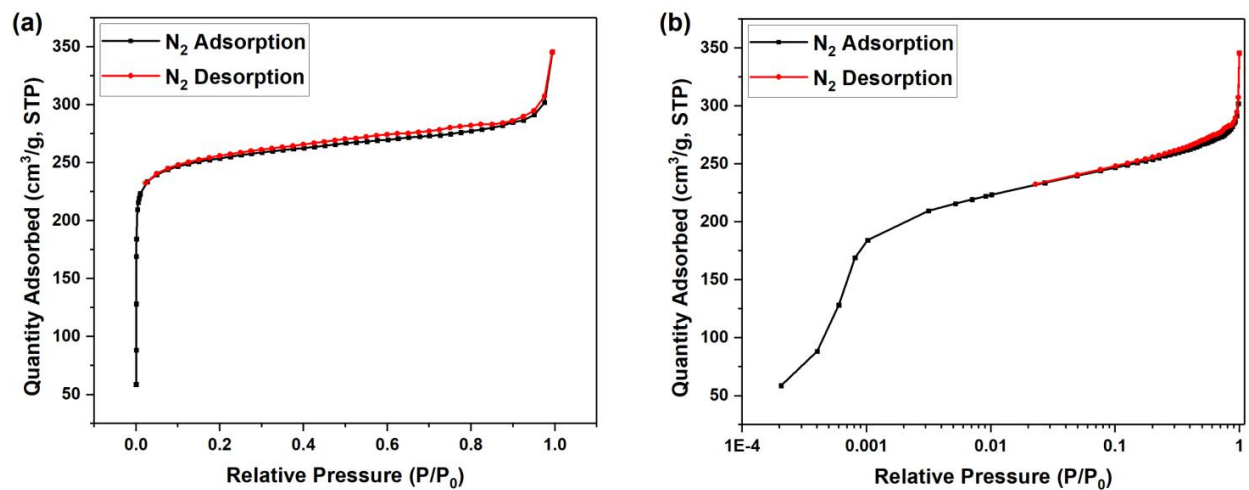
**PXRD patterns of ZEO-2 and ZEO-3:** (a) as-synthesized ZEO-2, (b) calcined ZEO-3 in air at 600 °C for 6 hours, (c) P-free ZEO-3 from H<sub>2</sub> reduction at 600 °C, (d) 800 °C calcined in air (with one-hour plateau) on the P-free ZEO-3, (e) 1100 °C calcined in air (with one-hour plateau) and (f) after hydrothermal treatment at 760 °C with 10% H<sub>2</sub>O vapor for 3 hours on the P-free ZEO-3.

**Fig. S10.**

5 **Cs-corrected STEM observations of ZEO-2 and ZEO-3.** Cs-corrected STEM observation of ZEO-2 along [110] (a-c). a) Low-magnification ADF micrograph. b) High-magnification ABF image (contrast inverted). c) Closer observation, ABF data, with FFT in the inset, where the systematic absences are pointed by red arrows.

10 Cs-corrected STEM-ADF observation of ZEO-3 along [110] (d-f). d) Low-magnification ADF micrograph. e) High-magnification ADF image. f) Atomic-resolution observation with FFT in the inset.

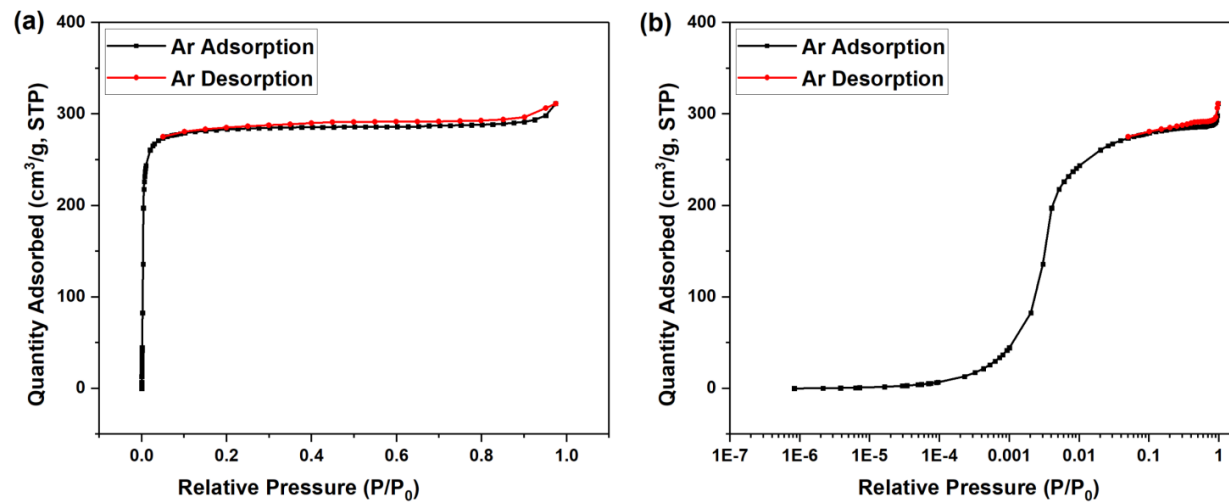
Cs-corrected STEM-ADF observation of ZEO-3 along [001] (g-i). g) Low-magnification ADF micrograph. h) High-magnification ADF image. i) Atomic-resolution observation with the FFT in the inset.



**Fig. S11.**

**N<sub>2</sub> adsorption/desorption isotherms of P-free ZEO-3 at 77 K, with x-axis in (a) linear and (b) logarithmic scale, respectively.**

5

**Fig. S12.**

**Ar adsorption/desorption isotherms of P-free ZEO-3 at 87 K, with x-axis in (a) linear and (b) logarithmic scale, respectively.**

5



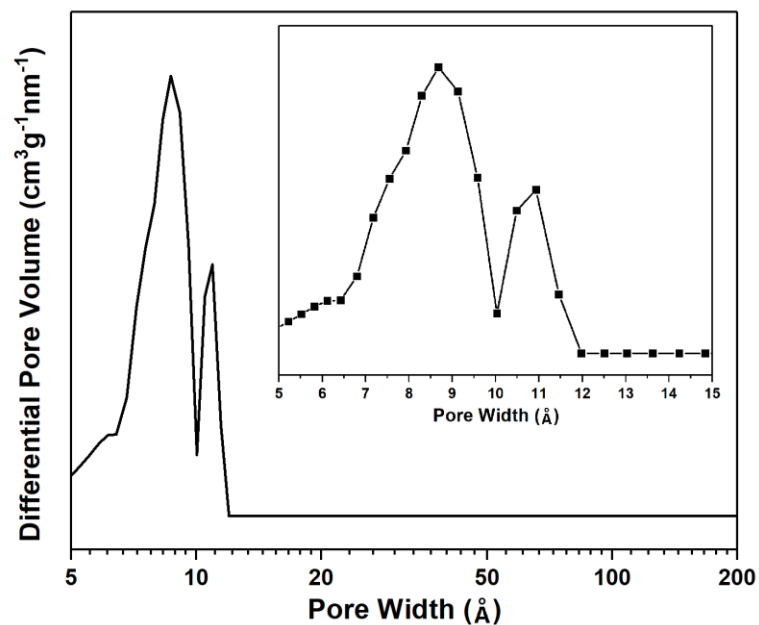


Fig. S13.

**Pore size distributions of P-free ZEO-3 from Ar adsorption isotherm at 87 K**, where the main figure shows the logarithmic scale of x-axis and the inserted figure shows the linear scale.

5

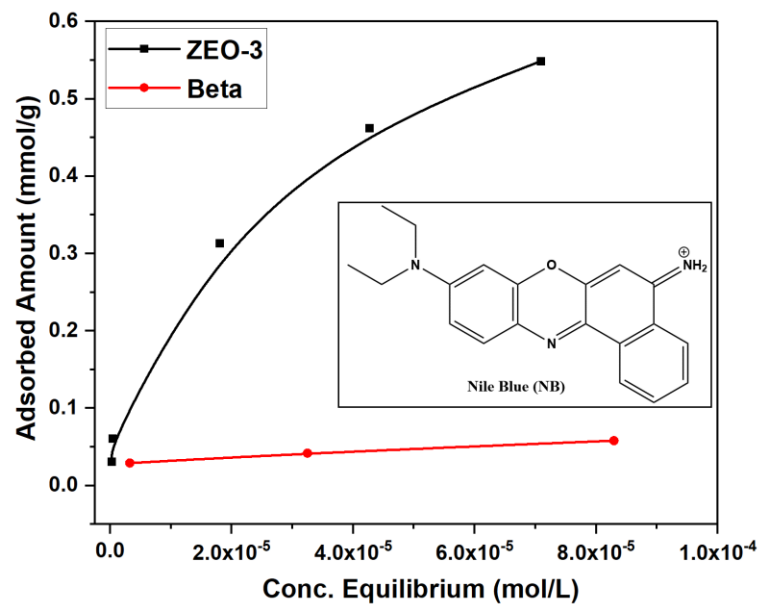
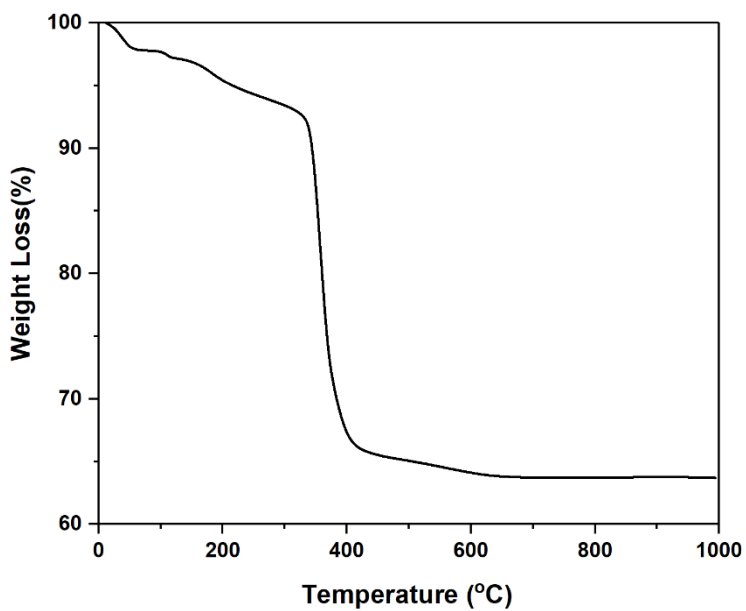


Fig. S14.

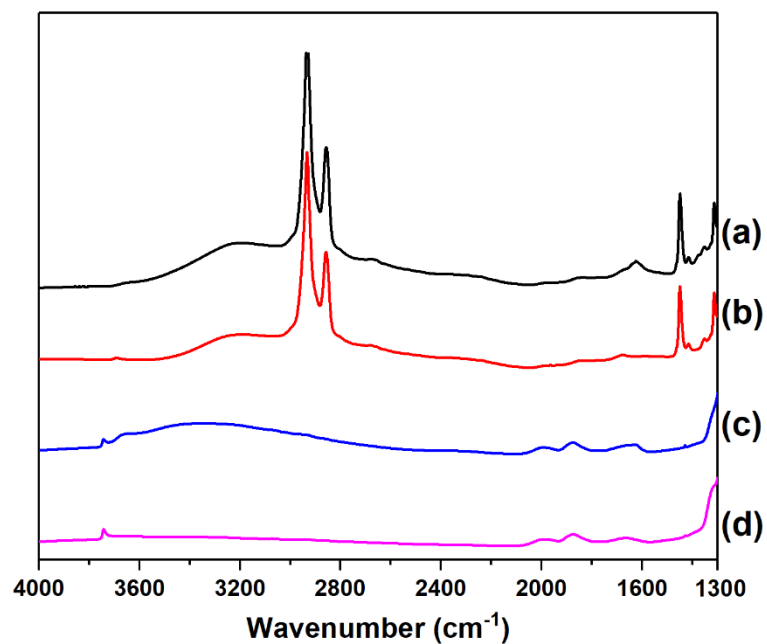
Nile Blue adsorption isotherms on the pure silica  $16 \times 14 \times 14$  MR ZEO-3 (black curve) and  $12 \times 12 \times 12$  MR Beta (red curve) zeolites, with the inserted figure of molecular structure of Nile Blue. These data show ZEO-3 has potential for the removal of large organic pollutants.



**Fig. S15.**

**Thermogravimetric curve of ZEO-2**, showing a weight loss of 4.59% and 31.71% in the range of RT-200 °C and 200-1000 °C, respectively.

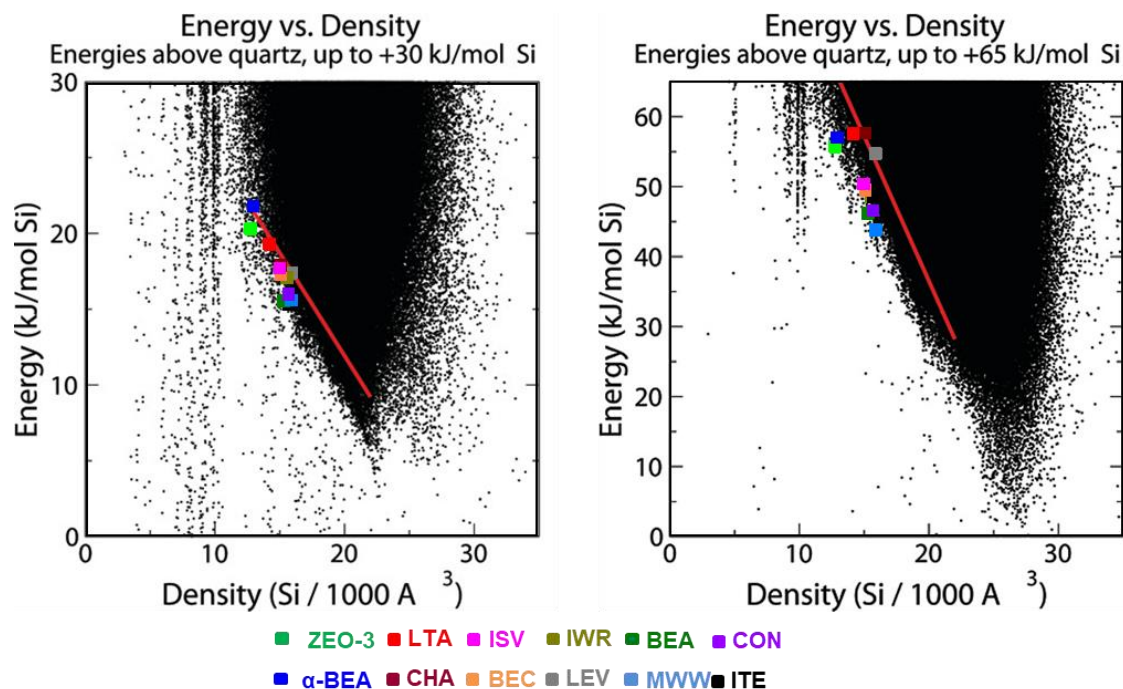
5



**Fig. S16.**

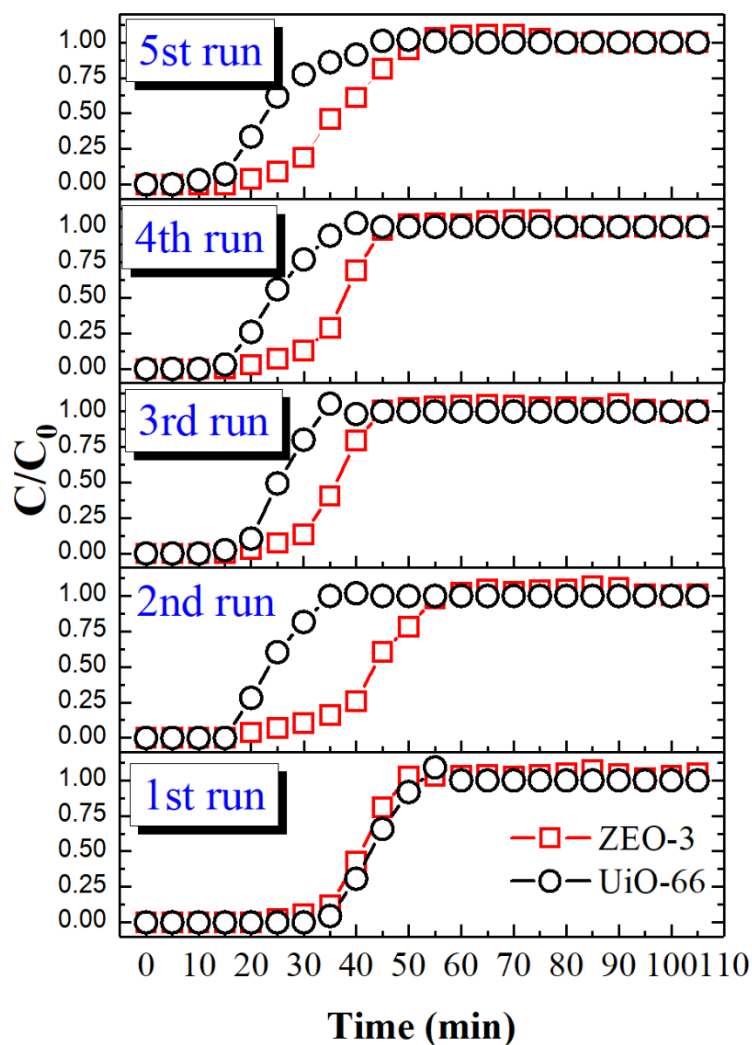
**FT-IR spectra of ZEO-2 and ZEO-3 from self-supported pellets:** (a) as-made ZEO-2, (b) ZEO-2 pellet dehydrated at 180 °C for 2 hours under vacuum, (c) calcined ZEO-3, and (d) ZEO-3 pellet dehydrated at 180 °C for 2 hours under vacuum.

5



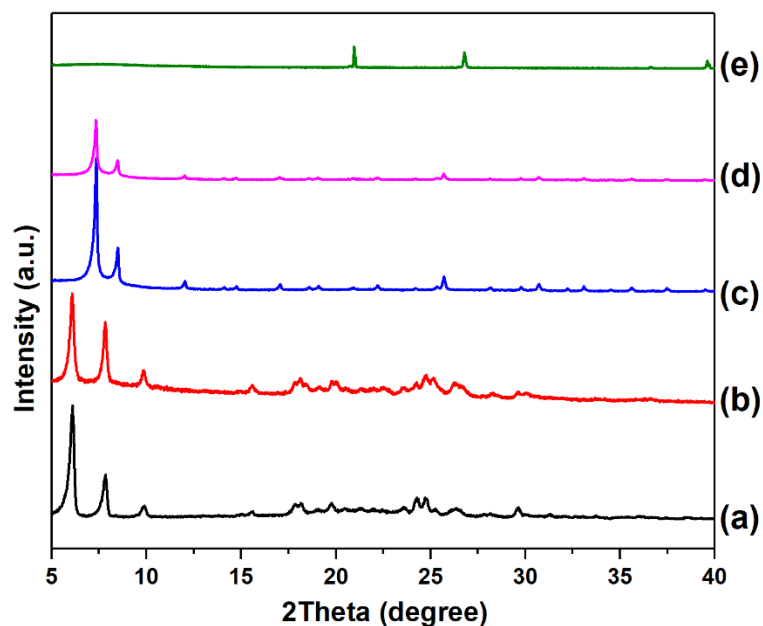
**Fig. S17.**

**Lattice energy versus density for the zeolite-like materials**, minimized by both the Sanders-Leslie-Catlow (SLC) and van Beest-Kramer-van Santen (BKS) interatomic potential, according to Deem et al (43). The red line appears in the original publication as "the linear fit of energy versus density for the known zeolite structures". We have included our data points for ZEO-3 (green), the hypothetical  $\sigma$ -BEA (blue) and ten highly porous crystalline silica polymorphs, calculated following the same methodology. Reprinted (adapted) with permission from M. W. Deem, R. Pophale, P. A. Cheeseman, D. J. Earl, Computational Discovery of New Zeolite-Like Materials, J. Phys. Chem. C, 2009, 113, 21353–21360. Copyright 2009 American Chemical Society.

**Fig. S18.**

**Successive cycles of VOC adsorption on ZEO-3 and UiO-66.** Fresh UiO-66 performs very similarly (1st run) but VOC adsorption on UiO-66 is severely compromised after regeneration in successive cycles due to structural degradation (see Fig. S19).

5



**Fig. S19.**

**PXRD patterns of UiO-66 and ZEO-3 used for VOC adsorption.** (a) Fresh H<sub>2</sub> reduced (P-free) ZEO-3, (b) ZEO-3 after VOC adsorption/desorption process, (c) commercial MOF UiO-66, (d) UiO-66 after pre-treatment of VOC process (see details in Supplementary Text) before the 1st run of VOC process, and (e) UiO-66 after VOC process. The starting UiO-66 material is highly crystalline and clearly identifiable as pure, maintains its structural integrity after the initial conditioning but has collapsed after the fifth cycle of VOC adsorption plus regeneration. ZEO-3, by contrast, withstands the whole process. The peaks in pattern (e) correspond to the added quartz (see details in Supplementary Text).

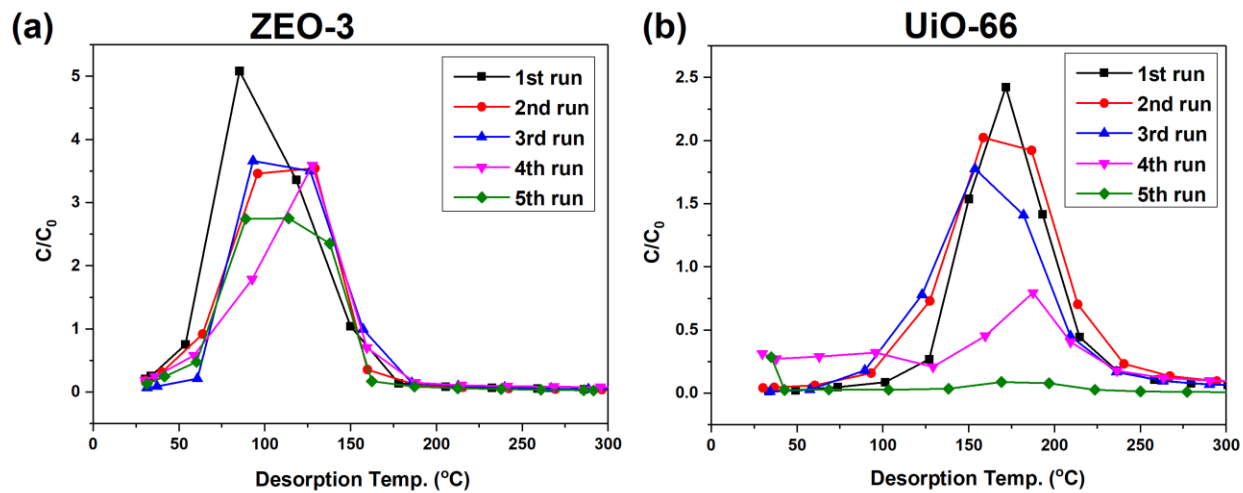
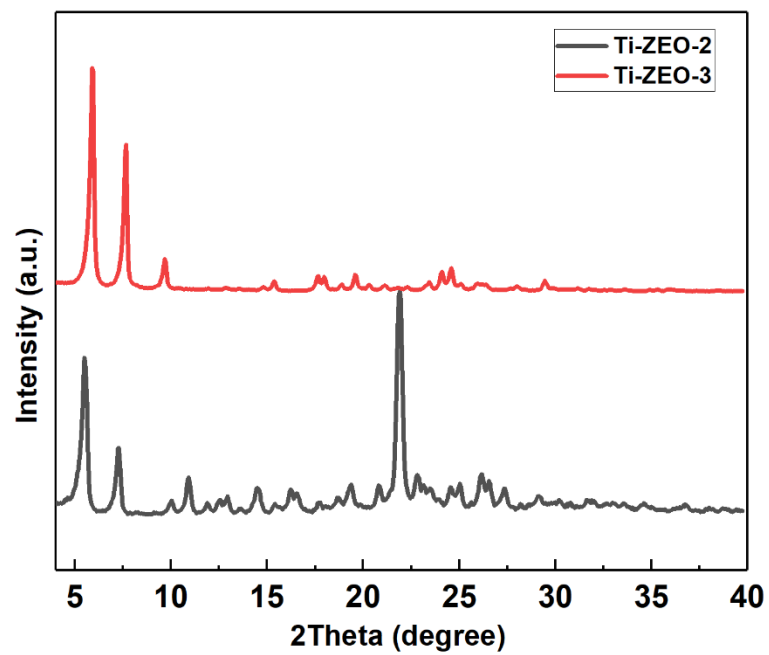


Fig. S20.

VOC desorption (adsorbent regeneration) curves from ZEO-3 and UiO-66. VOC desorption from ZEO-3 (a) occurs at significantly lower temperature than from UiO-66 (b).

5

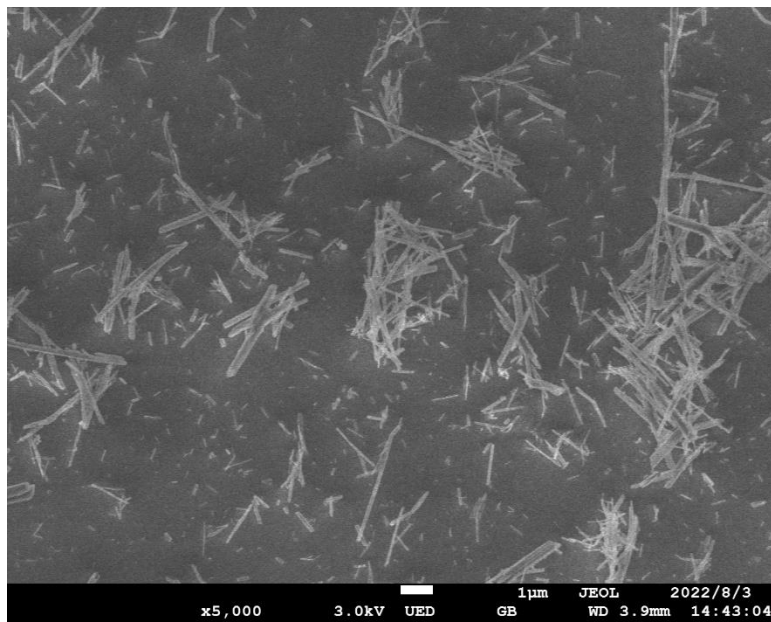




**Fig. S21.**

**PXRD patterns of the titanosilicate sample synthesized in this work:** Ti-ZEO-2 (black, bottom) and Ti-ZEO-3 (red, top).

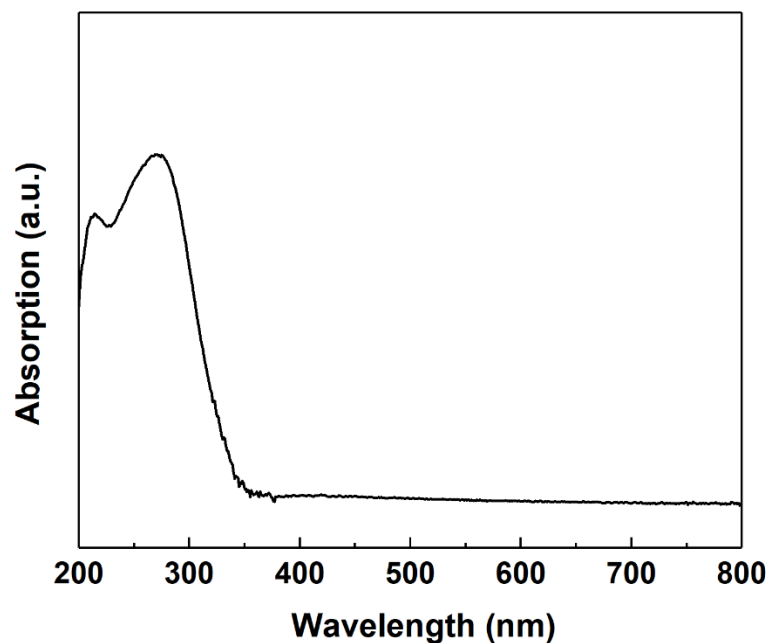
5



**Fig. S22.**

**FESEM images of the titanasilicate Ti-ZEO-3 sample synthesized in this work.**

5



**Fig. S23.**

**UV-vis spectrum of calcined Ti-ZEO-3 (Si/Ti 112 by ICP).** Please note that in addition to tetrahedrally coordinated Ti in framework positions (210-220 nm band), Ti-ZEO-3 also shows a band around 270 nm attributed to octahedral Ti, possibly in extraframework positions, featuring Ti-O-Ti bonds (44).

5

**Table S1.****cRED data indexing results for all crystals of ZEO-2.**

Data set	Space Group	$a/\text{\AA}$	$b/\text{\AA}$	$c/\text{\AA}$	$\alpha/^\circ$	$\beta/^\circ$	$\gamma/^\circ$	Volume/ $\text{\AA}^3$	Rotation Angle/ $^\circ$	Total Completeness/%
1	15	25.03	24.21	14.66	90	116.10	90	7977.11	65.1	48.9
2	15	25.37	24.3	14.93	90	117.21	90	8185.64	58.0136	40.1
3	15	24.44	24.52	14.51	90	119.59	90	7560.74	37.6974	30.2
4	15	25.49	24.79	14.69	90	113.91	90	8485.50	78.5512	65.2
5	15	24.65	24.31	14.44	90	115.98	90	7778.56	39.9803	30.9
6	15	25.66	24.14	14.92	90	117.05	90	8230.73	73.5332	48.6
7	15	24.09	25.14	14.3	90	115.00	90	7848.60	33.4656	27.6
8	15	24.44	25.33	14.5	90	115.46	90	8104.36	69.136	55

**Table S2.****cRED experimental parameters, crystallographic data, and structure refinement details of ZEO-2 and ZEO-3.**

<b>Experimental parameters and crystallographic data</b>		
Identification code	ZEO-2	ZEO-3
Number of datasets	8	5
Wavelength	0.0251 Å	0.0251 Å
Spot size	3	3
Rotation range per image (°)	0.23	0.23
Exposure time per image (s)	0.5	0.5
Program for data procession	<i>XDS</i>	<i>XDS</i>
Program for structure solution	ShelxT	ShelxT
Crystal system	Monoclinic	Monoclinic
Unit cell dimensions	$a = 25.164(5)$ Å $b = 24.761(5)$ Å $c = 14.818(3)$ Å $\beta = 116.55(3)^\circ$	$a = 22.362(5)$ Å $b = 22.147(4)$ Å $c = 14.920(3)$ Å $\beta = 108.26(3)^\circ$
Possible space group	<i>C2/c</i> , <i>Cc</i>	<i>C2/c</i> , <i>Cc</i>
Resolution	0.83	0.79
Completeness	92.2%	96.3%
$R_{\text{int}}$	42.71%	37.35%
No. of reflections	44258	36890
No. of unique reflections	6905	6471
<b>Structure refinement against cRED data</b>		
Formula <sup>[a]</sup>	Si <sub>80</sub> O <sub>176</sub>	Si <sub>80</sub> O <sub>160</sub>
Crystal system	Monoclinic	Monoclinic
Space group	<i>C2/c</i>	<i>C2/c</i>
Unit cell dimensions	$a = 25.164(5)$ Å $b = 24.761(5)$ Å $c = 14.818(3)$ Å $\beta = 116.55(3)^\circ$	$a = 22.362(5)$ Å $b = 22.147(4)$ Å $c = 14.920(3)$ Å $\beta = 108.26(3)^\circ$
<i>Z</i>	1	1
<i>F</i> (000)	1330	1194
Dataset ( <i>h</i> , <i>k</i> , <i>l</i> )	-26~29, -28~28, -17~16	-25~24, -24~27, -17~17
Total and unique data, $R_{\text{int}}$	44258, 6905, 42.71%	36890, 6471, 37.35%
Observed data [ $F_0 > 4\text{sig}(F_0)$ ]	1674	1665
$N_{\text{reflections}}$ , $N_{\text{parameters}}$ , $N_{\text{restraints}}$	44258, 108, 34	36890, 272, 31
$R_1$ , $wR_2$ , <i>Gof</i>	0.2595, 0.6808, 1.192	0.1963, 0.5202, 0.969
$I/\sigma$	2.9	3.1
$\rho_{\text{min}}$ , $\rho_{\text{max}}$ (e <sup>-</sup> /Å <sup>3</sup> )	-0.1/0.1	-0.2/0.2

[a] The hydrogens of the framework are omitted during the refinement of ZEO-2.

**Table S3.****cRED data indexing results for all crystals of ZEO-3.**

Data set	Space Group	$a/\text{\AA}$	$b/\text{\AA}$	$c/\text{\AA}$	$\alpha/^\circ$	$\beta/^\circ$	$\gamma/^\circ$	Volume/ $\text{\AA}^3$	Rotation Angle/ $^\circ$	Total Completeness/%
1	15	23.33	22.4	15.15	90	107.19	90	7563.35	93.190	66.6
2	15	22.72	22.32	15.12	90	110.69	90	7172.57	81.880	51.6
3	15	21.42	22.01	15.26	90	108.15	90	6836.27	65.191	42.7
4	15	22.78	21.79	15.18	90	107	90	7205.74	90.792	61.8
5	15	22.18	22.07	15.03	90	108.18	90	6989.74	82.076	44.2

**Table S4.****Rietveld refinement for ZEO-2 and ZEO-3.**

Identification code	ZEO-2	ZEO-3
Empirical formula <sup>[a]</sup>	[Si <sub>80</sub> O <sub>176</sub> ](C <sub>19</sub> H <sub>36</sub> P) <sub>8</sub>	Si <sub>80</sub> O <sub>160</sub>
Wavelength	0.457926 Å	0.457926 Å
Radiation	Synchrotron Radiation	Synchrotron Radiation
Crystal system	Monoclinic	Monoclinic
Space group	<i>C2/c</i>	<i>C2/c</i>
Unit cell dimensions	<i>a</i> = 23.5465(7) Å	<i>a</i> = 21.5046(8) Å
	<i>b</i> = 24.7446(7) Å	<i>b</i> = 21.2757(8) Å
	<i>c</i> = 14.4024(4) Å	<i>c</i> = 14.4638(4) Å
	$\beta$ = 115.1974(9)°	$\beta$ = 108.7196(15)°
Volume	7593.0(4) Å <sup>3</sup>	6267.5(4) Å <sup>3</sup>
<i>Z</i>	1	1
$2\theta$ range for data refinement	1° < $2\theta$ < 30°	1° < $2\theta$ < 30°
Number of parameters	174	113
Number of reflections	29046	29046
Number of data points	5748	4730
Number of restraints	46 for Si-O and 88 for O-Si-O and Si-O-Si	44 for Si-O and 86 for O-Si-O and Si-O-Si
Refinement method	Rietveld refinement	Rietveld refinement
<i>R<sub>p</sub></i> / <i>R<sub>wp</sub></i> / <i>R<sub>exp</sub></i> / <i>Gof</i>	0.0836/0.1056/0.068/2.25	0.0631/0.0789/0.0487/1.61

[a] The hydrogens of the framework are omitted during the refinement of ZEO-2.

**Table S5.****Atomic positions and multiplicity of ZEO-2 after Rietveld refinement.**

Atom	Element	Multiplicity	x	y	z	Occupancy
Si1	Si	8	0.4100(5)	0.4838(4)	0.6114(7)	1
Si3	Si	8	0.6424(5)	0.4380(4)	0.7402(7)	1
Si4	Si	8	0.4298(5)	0.3837(4)	0.3739(7)	1
Si5	Si	8	0.5074(5)	0.3950(4)	0.6100(7)	1
Si6	Si	8	0.3354(5)	0.4742(4)	0.3784(7)	1
Si8	Si	8	0.2838(5)	0.3469(4)	0.6137(7)	1
Si9	Si	8	0.3401(5)	0.2963(4)	0.3759(7)	1
Si10	Si	8	0.3728(4)	0.2587(4)	0.5992(7)	1
Si11	Si	8	0.2510(4)	0.3846(4)	0.3893(7)	1
Si2	Si	4	0.5	0.3030(5)	0.75	1
Si7	Si	4	0.5	0.4254(5)	0.25	1
O1	O	8	0.3186(8)	0.5254(7)	0.3037(13)	1
O2	O	8	0.4831(8)	0.3819(8)	0.4898(12)	1
O3	O	8	0.3666(8)	0.4948(6)	0.4935(14)	1
O4	O	8	0.3899(9)	0.3282(7)	0.3469(13)	1
O5	O	8	0.3843(9)	0.4351(8)	0.3589(13)	1
O6	O	8	0.4632(8)	0.3881(7)	0.2974(13)	1
O7	O	8	0.4578(8)	0.4341(7)	0.6254(13)	1
O8	O	8	0.2792(8)	0.3346(7)	0.3501(14)	1
O9	O	8	0.6808(8)	0.3837(7)	0.7854(13)	1
O10	O	8	0.5749(8)	0.4236(7)	0.6508(14)	1
O11	O	8	0.2719(10)	0.4411(8)	0.3579(13)	1
O12	O	8	0.4406(8)	0.2653(7)	0.6894(13)	1
O13	O	8	0.2779(8)	0.3807(8)	0.5128(13)	1
O14	O	8	0.6337(8)	0.4703(7)	0.8308(13)	1
O15	O	8	0.4502(8)	0.5373(7)	0.6606(12)	1
O16	O	8	0.4865(7)	0.3406(7)	0.8287(13)	1
O17	O	8	0.3232(9)	0.2917(7)	0.6260(13)	1
O18	O	8	0.2146(9)	0.3317(7)	0.6024(13)	1
O19	O	8	0.3725(8)	0.2819(7)	0.4954(13)	1
O20	O	8	0.3550(8)	0.1958(7)	0.5839(12)	1
O21	O	8	0.1759(8)	0.3814(7)	0.3386(12)	1
O22	O	8	0.3216(8)	0.2407(6)	0.3119(12)	1
C1	C	8	0.059(7)	-0.383(7)	-0.844(8)	0.626(3)
C2	C	8	0.087(6)	-0.413(7)	-0.759(7)	0.626(3)
C3	C	8	0.130(6)	-0.382(6)	-0.683(7)	0.626(3)
C4	C	8	0.103(3)	-0.338(3)	-0.668(5)	0.626(3)
C5	C	8	0.074(6)	-0.310(5)	-0.754(8)	0.626(3)
C6	C	8	0.033(7)	-0.339(6)	-0.827(8)	0.626(3)
P7	P	8	0.152(3)	-0.301(3)	-0.571(4)	0.626(3)



Template revised February 2021

C8	C	8	0.143(7)	-0.246(9)	-0.434(14)	0.626(3)
C9	C	8	0.121(3)	-0.291(3)	-0.488(4)	0.626(3)
C10	C	8	0.058(7)	-0.288(11)	-0.538(12)	0.626(3)
C11	C	8	0.032(6)	-0.282(10)	-0.472(11)	0.626(3)
C12	C	8	0.054(6)	-0.236(10)	-0.416(12)	0.626(3)
C13	C	8	0.118(6)	-0.237(9)	-0.368(13)	0.626(3)
C14	C	8	0.156(3)	-0.242(3)	-0.619(4)	0.626(3)
H15	H	8	0.089(7)	-0.373(7)	-0.871(8)	0.626(3)
H16	H	8	0.108(7)	-0.443(7)	-0.774(7)	0.626(3)
H17	H	8	0.147(6)	-0.404(6)	-0.623(7)	0.626(3)
H18	H	8	0.054(6)	-0.278(5)	-0.742(8)	0.626(3)
H19	H	8	-0.001(6)	-0.350(6)	-0.809(8)	0.626(3)
C20	C	8	0.223(3)	-0.324(2)	-0.509(4)	0.626(3)
H21	H	8	0.188(7)	-0.248(8)	-0.393(14)	0.626(3)
H22	H	8	0.044(7)	-0.260(11)	-0.586(13)	0.626(3)
H23	H	8	-0.013(6)	-0.279(11)	-0.508(11)	0.626(3)
H24	H	8	0.041(7)	-0.206(10)	-0.460(13)	0.626(3)
H25	H	8	0.132(7)	-0.203(8)	-0.332(13)	0.626(3)
C26	C	8	0.224(15)	-0.379(8)	-0.514(19)	0.626(3)
C27	C	8	0.282(14)	-0.398(8)	-0.460(19)	0.626(3)
C28	C	8	0.323(13)	-0.376(8)	-0.492(18)	0.626(3)
C29	C	8	0.322(12)	-0.324(7)	-0.488(16)	0.626(3)
C30	C	8	0.264(13)	-0.303(7)	-0.541(16)	0.626(3)
H31	H	8	0.210(15)	-0.391(8)	-0.584(19)	0.626(3)
H32	H	8	0.295(14)	-0.390(8)	-0.387(19)	0.626(3)
H33	H	8	0.364(12)	-0.391(9)	-0.449(18)	0.626(3)
H34	H	8	0.337(12)	-0.312(7)	-0.416(16)	0.626(3)
H35	H	8	0.266(12)	-0.265(6)	-0.529(15)	0.626(3)
H36	H	8	0.026(7)	-0.406(7)	-0.897(8)	0.626(3)
H37	H	8	0.056(6)	-0.426(6)	-0.738(7)	0.626(3)
H38	H	8	0.163(6)	-0.373(6)	-0.701(7)	0.626(3)
H39	H	8	0.069(6)	-0.350(5)	-0.647(7)	0.626(3)
H40	H	8	0.105(7)	-0.298(5)	-0.778(8)	0.626(3)
H41	H	8	0.014(7)	-0.318(6)	-0.890(8)	0.626(3)
H42	H	8	0.134(7)	-0.215(9)	-0.479(15)	0.626(3)
H43	H	8	0.133(6)	-0.321(9)	-0.441(12)	0.626(3)
H44	H	8	0.041(7)	-0.322(11)	-0.575(11)	0.626(3)
H45	H	8	0.042(6)	-0.312(10)	-0.423(10)	0.626(3)
H46	H	8	0.037(6)	-0.233(10)	-0.366(11)	0.626(3)
H47	H	8	0.131(6)	-0.265(8)	-0.317(12)	0.626(3)
H48	H	8	0.183(2)	-0.218(3)	-0.565(4)	0.626(3)
H49	H	8	0.173(3)	-0.247(3)	-0.668(4)	0.626(3)
H50	H	8	0.115(2)	-0.227(3)	-0.653(4)	0.626(3)
H51	H	8	0.237(14)	-0.314(7)	-0.438(17)	0.626(3)
H52	H	8	0.195(16)	-0.395(8)	-0.49(2)	0.626(3)

Template revised February 2021

H53	H	8	0.282(15)	-0.437(9)	-0.47(2)	0.626(3)
H54	H	8	0.311(13)	-0.389(8)	-0.562(18)	0.626(3)
H55	H	8	0.349(11)	-0.309(7)	-0.515(16)	0.626(3)
H56	H	8	0.251(13)	-0.309(7)	-0.614(16)	0.626(3)
BC1	C	8	-0.686(8)	-0.010(7)	-1.115(12)	0.374(2)
BC2	C	8	-0.652(7)	0.022(7)	-1.019(12)	0.374(2)
BC3	C	8	-0.606(7)	-0.014(6)	-0.936(11)	0.374(2)
BC4	C	8	-0.563(4)	-0.039(6)	-0.973(8)	0.374(2)
BC5	C	8	-0.597(7)	-0.070(7)	-1.069(11)	0.374(2)
BC6	C	8	-0.641(7)	-0.035(7)	-1.149(11)	0.374(2)
BP7	P	8	-0.501(3)	-0.080(6)	-0.873(7)	0.374(2)
BC8	C	8	-0.399(4)	-0.08(3)	-0.920(12)	0.374(2)
BC9	C	8	-0.423(3)	-0.052(5)	-0.851(7)	0.374(2)
BC10	C	8	-0.427(5)	0.01(2)	-0.870(10)	0.374(2)
BC11	C	8	-0.365(6)	0.03(2)	-0.850(9)	0.374(2)
BC12	C	8	-0.339(5)	0.00(2)	-0.918(9)	0.374(2)
BC13	C	8	-0.337(4)	-0.06(2)	-0.904(11)	0.374(2)
BC14	C	8	-0.507(3)	-0.147(6)	-0.924(6)	0.374(2)
BH15	H	8	-0.715(9)	-0.041(7)	-1.103(13)	0.374(2)
BH16	H	8	-0.687(8)	0.037(8)	-0.994(12)	0.374(2)
BH17	H	8	-0.581(6)	0.011(6)	-0.872(11)	0.374(2)
BH18	H	8	-0.565(6)	-0.088(8)	-1.095(10)	0.374(2)
BH19	H	8	-0.617(6)	-0.004(7)	-1.170(11)	0.374(2)
BC20	C	8	-0.505(3)	-0.085(5)	-0.750(7)	0.374(2)
BH21	H	8	-0.392(3)	-0.12(2)	-0.903(14)	0.374(2)
BH22	H	8	-0.459(6)	0.02(3)	-0.945(10)	0.374(2)
BH23	H	8	-0.368(6)	0.07(2)	-0.865(9)	0.374(2)
BH24	H	8	-0.368(6)	0.01(3)	-0.996(9)	0.374(2)
BH25	H	8	-0.320(4)	-0.08(3)	-0.956(11)	0.374(2)
BC26	C	8	-0.51(4)	-0.142(6)	-0.72(3)	0.374(2)
BC27	C	8	-0.51(4)	-0.146(5)	-0.62(3)	0.374(2)
BC28	C	8	-0.46(4)	-0.117(6)	-0.54(3)	0.374(2)
BC29	C	8	-0.46(4)	-0.061(6)	-0.57(3)	0.374(2)
BC30	C	8	-0.45(4)	-0.055(7)	-0.67(3)	0.374(2)
BH31	H	8	-0.47(4)	-0.163(6)	-0.71(3)	0.374(2)
BH32	H	8	-0.56(4)	-0.129(5)	-0.63(3)	0.374(2)
BH33	H	8	-0.47(4)	-0.120(5)	-0.47(3)	0.374(2)
BH34	H	8	-0.50(4)	-0.040(6)	-0.57(3)	0.374(2)
BH35	H	8	-0.46(4)	-0.014(7)	-0.68(3)	0.374(2)
BH36	H	8	-0.718(8)	0.017(8)	-1.175(13)	0.374(2)
BH37	H	8	-0.629(7)	0.055(7)	-1.035(11)	0.374(2)
BH38	H	8	-0.630(7)	-0.043(6)	-0.915(11)	0.374(2)
BH39	H	8	-0.537(5)	-0.007(6)	-0.992(10)	0.374(2)
BH40	H	8	-0.623(7)	-0.102(7)	-1.055(11)	0.374(2)
BH41	H	8	-0.667(8)	-0.059(8)	-1.217(12)	0.374(2)

Template revised February 2021

BH42	H	8	-0.431(4)	-0.07(3)	-0.999(12)	0.374(2)
BH43	H	8	-0.391(4)	-0.06(2)	-0.774(12)	0.374(2)
BH44	H	8	-0.443(5)	0.03(2)	-0.818(10)	0.374(2)
BH45	H	8	-0.331(5)	0.02(2)	-0.771(9)	0.374(2)
BH46	H	8	-0.293(6)	0.02(2)	-0.899(8)	0.374(2)
BH47	H	8	-0.303(4)	-0.07(2)	-0.828(11)	0.374(2)
BH48	H	8	-0.470(3)	-0.172(5)	-0.870(6)	0.374(2)
BH49	H	8	-0.551(3)	-0.164(6)	-0.938(7)	0.374(2)
BH50	H	8	-0.502(3)	-0.146(6)	-0.994(6)	0.374(2)
BH51	H	8	-0.55(4)	-0.066(6)	-0.76(3)	0.374(2)
BH52	H	8	-0.55(4)	-0.163(6)	-0.78(3)	0.374(2)
BH53	H	8	-0.51(4)	-0.188(5)	-0.60(3)	0.374(2)
BH54	H	8	-0.42(4)	-0.138(6)	-0.52(3)	0.374(2)
BH55	H	8	-0.42(4)	-0.041(6)	-0.51(3)	0.374(2)
BH56	H	8	-0.41(4)	-0.070(7)	-0.65(3)	0.374(2)

---

**Table S6.****Si-O bond distances (Å) for ZEO-2.**

Si1-O3	1.589(1)	Si6-O1	1.599(1)
Si1-O7	1.621(2)	Si6-O3	1.585(1)
Si1-O15	1.606(1)	Si6-O5	1.621(2)
Si1-O14	1.611(2)	Si6-O11	1.621(3)
Si2-O12	1.597(1)	Si7-O6	1.604(1)
Si2-O16	1.599(1)	Si7-O6	1.604(1)
Si2-O12	1.597(1)	Si7-O15	1.612(1)
Si2-O16	1.599(1)	Si7-O15	1.612(1)
Si3-O9	1.596(1)	Si8-O13	1.631(1)
Si3-O10	1.603(1)	Si8-O17	1.621(2)
Si3-O14	1.616(1)	Si8-O18	1.611(2)
Si3-O1	1.601(2)	Si8-O9	1.614(1)
Si4-O2	1.606(1)	Si9-O4	1.611(2)
Si4-O4	1.621(2)	Si9-O8	1.621(2)
Si4-O5	1.621(2)	Si9-O19	1.598(1)
Si4-O6	1.607(1)	Si9-O22	1.609(1)
Si5-O2	1.608(1)	Si10-O12	1.580(1)
Si5-O7	1.601(2)	Si10-O17	1.601(2)
Si5-O10	1.611(2)	Si10-O19	1.599(1)
Si5-O16	1.582(1)	Si10-O20	1.601(2)
Si11-O8	1.621(2)	Si11-O13	1.617(9)
Si11-O11	1.611(2)	Si11-O21	1.601(2)

**Table S7.****Bond angles for ZEO-2.**

Bond Angles (°)	Min	Max
Si-O-Si	134.1(1)	161.6(1)
O-Si-O	107.3(9)	111.7(1)

**Table S8.****Atomic positions and multiplicity of ZEO-3 after Rietveld refinement.**

Atom	Element	Multiplicity	<i>x</i>	<i>y</i>	<i>z</i>	Occupancy
Si1	Si	8	0.4110(5)	0.5232(4)	0.6310(7)	1
Si2	Si	8	0.7709(5)	0.1730(5)	0.6486(7)	1
Si4	Si	8	0.8278(5)	0.0340(4)	0.4072(8)	1
Si5	Si	8	0.6609(6)	0.2620(5)	0.5821(8)	1
Si7	Si	8	0.5730(5)	0.3607(5)	0.6152(7)	1
Si8	Si	8	0.5089(5)	0.6298(4)	0.6103(7)	1
Si9	Si	8	0.8493(5)	0.9255(4)	0.2857(7)	1
Si10	Si	8	0.7425(5)	0.1318(5)	0.4417(6)	1
Si11	Si	8	0.6306(5)	0.2200(5)	0.3727(6)	1
Si3	Si	4	0.5	0.7401(7)	0.75	1
Si6	Si	4	0.5	0.4158(6)	0.75	1
O1	O	8	0.7103(1)	0.2143(8)	0.6543(13)	1
O2	O	8	0.6084(9)	0.2933(8)	0.6253(11)	1
O3	O	8	0.7621(9)	0.0665(8)	0.4041(13)	1
O4	O	8	0.8659(9)	0.0119(8)	0.5176(14)	1
O5	O	8	0.7977(1)	0.1296(8)	0.7435(1)	1
O6	O	8	0.8627(9)	0.9581(8)	0.1914(1)	1
O7	O	8	0.7421(9)	0.1302(9)	0.5518(1)	1
O8	O	8	0.5415(8)	0.3701(8)	0.7004(1)	1
O9	O	8	0.5606(1)	0.2149(8)	0.2902(1)	1
O10	O	8	0.8140(9)	0.9755(8)	0.3370(1)	1
O11	O	8	0.8730(9)	0.0823(9)	0.3716(1)	1
O12	O	8	0.4629(1)	0.5809(8)	0.6431(1)	1
O13	O	8	0.5168(1)	0.3620(9)	0.5089(1)	1
O14	O	8	0.4496(9)	0.4589(9)	0.6670(1)	1
O15	O	8	0.6737(1)	0.1589(9)	0.3760(1)	1
O16	O	8	0.6246(9)	0.2264(7)	0.4801(1)	1
O17	O	8	0.5085(9)	0.6978(9)	0.6629(1)	1
O18	O	8	0.6676(1)	0.2823(8)	0.3548(1)	1
O19	O	8	0.7017(1)	0.3189(8)	0.5593(1)	1
O20	O	8	0.5834(1)	0.6032(8)	0.6370(1)	1

**Table S9.****Si-O bond distances (Å) for ZEO-3.**

Si1-O12	1.630(1)	Si6-O8	1.633(1)
Si1-O14	1.601(2)	Si6-O14	1.619(1)
Si1-O4	1.631(2)	Si6-O8	1.633(1)
Si1-O6	1.611(2)	Si6-O14	1.619(1)
Si2-O1	1.596(1)	Si7-O2	1.611(2)
Si2-O5	1.600(1)	Si7-O8	1.598(1)
Si2-O7	1.618(1)	Si7-O13	1.623(1)
Si2-O18	1.643(1)	Si7-O11	1.651(2)
Si3-O17	1.606(1)	Si8-O12	1.609(1)
Si3-O17	1.606(1)	Si8-O17	1.636(1)
Si3-O9	1.571(1)	Si8-O20	1.625(1)
Si3-O9	1.571(1)	Si8-O13	1.642(1)
Si4-O3	1.561(2)	Si9-O6	1.636(1)
Si4-O4	1.611(2)	Si9-O10	1.619(1)
Si4-O11	1.611(2)	Si9-O5	1.595(1)
Si4-O10	1.573(1)	Si9-O20	1.637(1)
Si5-O1	1.593(1)	Si10-O3	1.601(2)
Si5-O2	1.601(2)	Si10-O7	1.596(1)
Si5-O16	1.619(1)	Si10-O15	1.588(1)
Si5-O19	1.591(1)	Si10-O19	1.597(1)
Si11-O9	1.597(1)	Si11-O16	1.605(1)
Si11-O15	1.588(1)	Si11-O18	1.609(1)

**Table S10.****Bond angles for ZEO-3.**

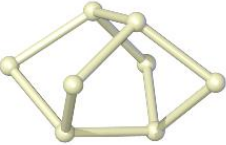
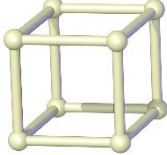
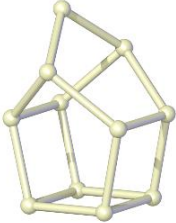
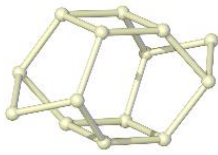
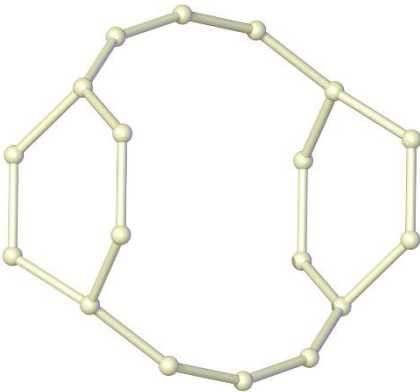
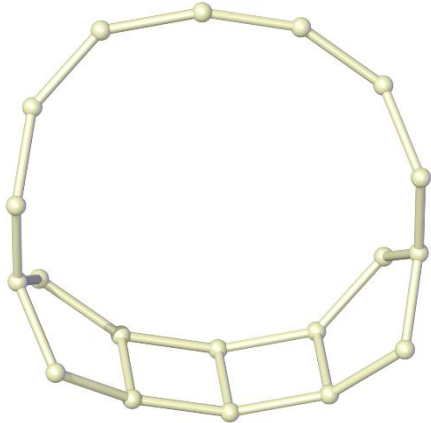

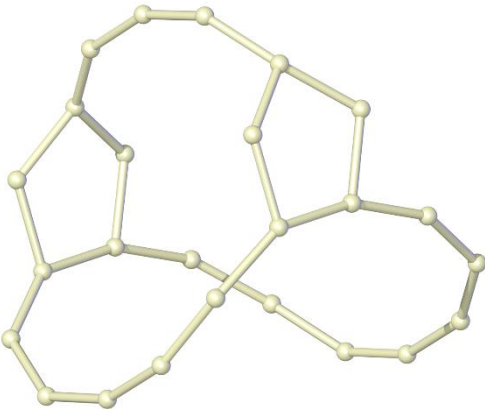
Bond Angles (°)	Min	Max
Si-O-Si	134.5(1)	165.4(8)
O-Si-O	104.9(1)	114.5(1)



**Table S11.****Coordination sequences and vertex symbols of ZEO-3.**

	N1	N2	N3	N4	N5	N6	N7	N8	N9	N10	N11	N12	Vertex symbol
T1	4	11	18	27	34	54	81	113	140	159	181	224	4.5(2).5.5.5.6
T2	4	10	19	27	39	53	80	109	139	166	192	224	4.6.4.14.5.5
T3	4	8	15	26	39	55	73	102	135	169	194	227	4.4.4.5.4.14(5)
T4	4	10	19	28	38	54	77	111	140	166	191	224	4.6.4.14(5).5.5
T5	4	11	18	25	36	54	85	110	134	157	188	230	4.5(2).5.5.5.6
T6	4	12	17	25	38	58	80	113	135	156	192	231	5.5.5.6.5(2).14(3)
T7	4	8	15	26	38	54	76	105	131	165	196	228	4.4.4.5.4.14
T8	4	9	15	24	39	57	80	103	127	156	204	240	4.5.4.5.4.14
T9	4	12	15	22	40	62	84	107	122	152	200	250	5.5.5.5.5(2).16(9)
T10	4	12	19	28	36	52	82	115	144	162	186	218	5.5.5(2).14(6).6.6
T11	4	9	15	25	40	55	77	102	134	163	196	229	4.5.4.5.4.14(5)

**Table S12.****Tiling of ZEO-3.**

Tiling of ZEO-3: $[5^4] + [4^2.16^2] + [6^2.14^2] + 2[5^2.14.16^2] + [4^6] + 2[4^2.5^2.14^2] + 2[4^3.5^4] + [4^2.5^4.6^2]$ . Transitivity: (11) (20) (16) 8.			
$[5^4]$ , <i>mor</i>	$[4^6]$ , <i>d4r</i>	$[4^3.5^4]$ , <i>bea</i>	$[4^2.5^4.6^2]$ , <i>mtw</i>
			
(8, 10, 4)	(8, 12, 6)	(11, 16, 7)	(14, 20, 8)
$[6^2.14^2]$		$[4^2.5^2.14^2]$	
			
(18, 20, 4)		(19, 23, 6)	
$[4^2.16^2]$		$[5^2.14.16^2]$	
			
(18, 20, 4)		(25, 28, 5)	

**Table S13.**

**Framework density (FD, number of T-atoms per 1000 Å<sup>3</sup>) of quartz and highly porous crystalline silica polymorphs<sup>[a]</sup>.**

Phase	FD <sup>[b]</sup>	FD <sub>Si</sub> <sup>[c]</sup>	Ref.
Quartz	26.41	-	(45)
<b>*BEA</b>	-	15.3	
<b>BEC</b>	-	15.1	
<b>CHA</b>	15.4	15.1	(46)
<b>CON</b>	16.07	15.7	(47)
<b>ISV</b>	15.37	15.0	(48)
<b>ITE</b>	16.3	15.7	(49)
<b>IWR</b>	15.5	15.6	(50)
<b>LEV</b>	15.2	15.9	(51)
<b>LTA</b>	14.40	14.2	(52)
<b>MWW</b>	16.51	15.9	(53)
ZEO-3	12.76	-	this work

5 [a] Crystalline SiO<sub>2</sub> polymorphs with FD (experimental or calculated) < 16 Si/1000 Å<sup>3</sup>. [b] Experimental FD, when available, according to the data in the reference in last column. [c] FD of a geometrically optimized SiO<sub>2</sub> framework (according to the IZA website) (51).

**Table S14.****Potential parameters used in the framework energy minimization.**

<b>Potential parameters for the polarizable Sanders-Leslie-Catlow (SLC) interatomic potential <sup>[a]</sup></b>				
<b>Buckingham potential</b>				
<b>i...j</b>	<b>A<sub>ij</sub> (eV)</b>	<b>ρ<sub>ij</sub>(Å)</b>	<b>C<sub>ij</sub>(eVÅ<sup>6</sup>)</b>	<b>Atomic charge</b>
Si <sup>4+</sup> ...O <sup>2-</sup>	1283.907	0.32052	10.66158	qSi =4.0
O <sup>2-</sup> ...O <sup>2-</sup>	22764.0	0.149	27.88	qO <sup>2-</sup> <sub>core</sub> = 0.86902 qO <sup>2-</sup> <sub>shell</sub> = -2.86902
<b>Three-body potential</b>				
	<b>k (eV rad<sup>-1</sup>)</b>	<b>θ(deg)</b>		
O-T-O	2.09724	109.47		
<b>Core-shell</b>				
	<b>k (eVÅ<sup>-1</sup>)</b>			
O <sup>2-</sup>	74.92			
<b>Potential parameters for the nonpolarizable van Beest-Kramer-van Santen (BKS) interatomic potential <sup>[b]</sup></b>				
<b>i...j</b>	<b>A<sub>ij</sub> (eV)</b>	<b>ρ<sub>ij</sub>(Å)</b>	<b>C<sub>ij</sub>(eVÅ<sup>6</sup>)</b>	<b>Atomic charges</b>
O-O	1388.773	0.36231	175.000	qO=-1.2
Si-O	18003.7572	0.20906	133.5381	qSi=2.4

5 The interatomic potentials combine long-range Coulomb term with short-range pair interactions.

$$\Phi_{ij} = \frac{q_i q_j}{r_{ij}} + A_{ij} \exp\left(\frac{-r_{ij}}{\rho}\right) - C_{ij} r_{ij}^{-6}$$

$\Phi_{ij}$  is the interaction energy of atoms i and j, which consists of a Coulomb term and a covalent (short-range) contribution, cast into the usual Buckingham form.

10 [a] The long-range Coulomb term uses formal charges and the short-range two-body term is of the Buckingham type and the cut-off radius for the short-range interaction was 12 Å, and a three-body bond-bending term is used for O-Si-O groups. To allow polarization of the oxygen ions, the shell model is adopted. This describes the polarizable atom in terms of a core (in which the mass of the atom is concentrated) and a shell (describing the polarizable valence-shell electrons) which are

15 connected by a harmonic spring. Because the shells overlapping in the polarizable SLC interatomic potential, the structures are re-optimized twice with new shell positions,

[b] It allows for only two different short-range interactions: Si-O to describe the silica bond and the O-O nonbonded interaction, which modifies the Coulomb repulsion and ensures the tetrahedral arrangement of oxygen atoms around the silicon atom.

20